A machine learning-based perspective on deep convective clouds and their organisation in 3D. Part I: Influence of deep convective cores on the cloud life-cycle

Sarah Brüning[1] and Holger Tost[1]

[1]Institute for Physics of the Atmosphere, Johannes Gutenberg University Mainz, Johann-Joachim-Becher-Weg 21, Mainz, 55128, Rhineland-Palatinate, Germany

Correspondence: Sarah Brüning (sbruenin@uni-mainz.de)

Abstract. In this two-part ~~sequence of papers, we investigate~~ study, we examine spatio-temporal patterns of convective ~~cloud activity~~ clouds, their properties, and organisation. ~~The analysis employs a machine learning (ML)-based~~ We use a machine learning-based method to extrapolate a contiguous 3D ~~extrapolation of satellite data from multiple sensors to simultaneously follow~~ cloud field of 2D satellite data. The predicted data are used to simultaneously track both the horizontal and vertical ~~cloud development . Our study covers~~ development of clouds. Our research focuses on West Africa, a ~~hotspot for intense convection~~ region known for frequent convective events and severe weather. In ~~this part, we derive seasonal and diurnal variations for convective cloud properties during spring (March–May) and summer (June–August). Moreover, we explore the connection between the number of deep convective cores (DCCs)~~ Part 1, this study compares cloud and core properties and the cloud life-cycle ~~. For that purpose, we track the evolution of convective systems and their core regions. More than 80 % of detected clouds contain a single convective~~ over land and ocean during a six-month period from March to August 2019. Our analysis reveals that 65 % of tracked cloud systems contain only a single core and persist ~~between 1–3 hours. These isolated clouds have an enhanced absolute cooling but weaker anvil growth and updraft strength during their growthstage than clustered systems. The average difference between oceanic and continental cloud properties accounts for about~~ for less than three hours. Despite their shorter lifespan compared to multi-core clusters, single-core clouds exhibit stronger changes in the radar reflectivity and a higher vertical growth. In contrast, multi-core clouds show greater horizontal growth, encompassing larger cloud and core areas, higher cloud-top heights (CTH), and higher average reflectivity at 10 ~~%. However, we detect a high seasonal variability and a surface-specific diurnal cycle. We find long-lasting cloud clusters with more intense core regions over continental Africa. Within these clusters, the interaction between cores may renew convective activity. The horizontal growth of convective clouds is about 5–10 % more intense over land in both seasons, even though convective activity over the ocean increases stronger in summer. While our results emphasise an enhanced convective activity over land, we suggest further analysis of regional patterns of clustered convectionand their hydro-climatological impact~~km altitude. We also find that, in systems with more cores, both the maximum number of cores and the peak core area occur later during the cloud life-cycle. Notably, the differences in cloud characteristics between land and ocean are smaller than those associated with the number of convective cores. However, the results may not fully capture climatological differences. Further research using longer time series is needed to quantify the observed variability of tropical convection.

Copyright statement.

1 Introduction

Convective clouds ~~substantially impact~~ play a vital role in the hydrological cycle of the Earth through their radiative forcing and feedback mechanisms ~~(Roca et al., 2010). Research shows that clouds may enhance climate warming. However, they are still regarded as~~ (Wielicki et al., 1995). Despite growing evidence for the connection between clouds and climate warming, they remain one of the ~~largest~~ greatest sources of uncertainty ~~for climate sensitivity studies (Chen et al., 2021).Moreover~~in climate sensitivity assessments (e.g., Bony et al. (2015); Sherwood et al. (2020)). Additionally, convective clouds are ~~major producers~~ key drivers of severe weather~~(Kukulies et al., 2021; Haberlie and Ashley, 2018). Large-scale cloud clusters,~~ , particularly large-scale systems like mesoscale convective systems (MCSs), ~~are responsible for extreme weather~~ which are linked to extreme events such as ~~hail, strong~~ hailstorms, damaging winds, and ~~extreme precipitation (Prein et al., 2024).Due to this threat for society and nature, an accurate representation of~~ intense rainfall (e.g., Houze and Hobbs (1982); Leary and Houze (1980); Maddox (1980)). Because of their societal and environmental impacts, accurately representing convective clouds remains of particular interest~~(Guillaume et al., 2018)~~.

~~Houze Jr. (2004) defined a MCS as a convective storm complex~~ MCSs are typically defined as convective storm complexes with an axis length of at least 100 km ~~and more. Typically, it consists of a contiguous~~ (Houze Jr., 2004). These systems often feature a broad cold cloud shield~~composed of~~ , one or more deep convective cores (~~DCCs~~hereafter, "cores"), strong vertical updrafts that ~~merge the~~ connect these cores at higher altitudes~~(Zipser and LeMone, 1980), and large anvils flowing out from the region of convective activity (Horner and Gryspeerdt, 2023). By counting the number of DCCs, we can approximate the degree of convective organisation. Higher numbers of DCCs come along with a stronger organisation, which, in turn, enhances the potential hazard of the cluster (Jones et al., 2024). For instance, DCCs are drivers of intense precipitation. In contrast~~, and widespread anvils extending from the convective region (Zipser and LeMone, 1980). While cores drive intense precipitation, the stratiform anvil and cirrus canopy ~~produce only lighter rain (Houze Jr., 2004).The size of a DCC ranges between~~ generally produce lighter rain (e.g., Houze Jr. (1989); Hartmann et al. (1984)). Core sizes typically range from 10 ~~–~~ to 100 km~~with an average lifetime of up to~~ , with lifespans of 1–3 ~~h, whereas the cloud anvil can persist~~ hours, whereas anvils can persist for up to 10–20 ~~h or longer (Chen and Houze, 1997). We observe an idealised~~ hours. The idealised MCS life-cycle ~~that can be divided into~~ includes three stages: ~~the convective initiation (CI), the maturityphase (MAT), and the dissipation of the cloud (Fiolleau and Roca, 2013). Deep convective cells are triggered during the CI to bring the condensate upwards~~development, maturity, and dissipation (Futyan and Genio, 2007). During development, deep convective cells form and transport condensate upward. In the maturity stage, the ~~stratiform~~ anvil and associated mesoscale circulation ~~build up while deep convective cells still exist~~develop while convection continues. In the dissipation stage, deep convection ~~stops~~ceases, and the ~~cloud slowly fades out (Houze and Hobbs, 1982). The life-cycle of an MCS is connected to the location, daytime~~ system gradually fades (e.g., Houze and Hobbs (1982); Machado et al. (1998)). The MCS life-cycle is influenced by location, time of day, and surface type~~(Houze Jr., 2004). Small and medium-sized MCSs over land occur most frequently~~ . For instance, small

to medium MCSs commonly form over land in the afternoon ~~. This peak is associated with~~ due to local thermal instability and~~(given the underlying surface properties potentially) a sea breeze circulation. Over the sea, we detect a weak semi-diurnal variability caused by the thermal properties of the underlying surfaceand the local circulation (Li et al., 2021). The structure and associated precipitation of MCSs differ with the region of genesis, e.g., when comparing the tropics and mid-latitudes (Kukulies et al., 2021)~~, potentially, sea breeze circulations (Chen and Houze, 1997). In contrast, oceanic MCSs experience weaker diurnal variability because of the surface's stable thermal properties (Nesbitt and Zipser, 2003).

~~Most of our~~ Our current understanding of convective clouds ~~originates from observational data (Haynes et al., 2009). Remote sensing instruments provide highly-resolved data that help investigate the temporal evolution of MCSs (Bacmeister and Stephens, 2011) , contributing towards a more realistic representation of cloud feedback mechanisms in climate models (Chen et al., 2021). Data from~~ largely stems from satellite observations (Haynes et al., 2009). We may identify convective clouds from satellite data by distinguishing core regions and the surrounding cloud field (Steiner et al., 1995). Cores are typically characterised by cold peaks in brightness temperature, surrounded by warmer anvil regions. Morphological features such as aspect ratio, length, width, and area may further classify convective systems (Ganetis et al., 2018). For instance, passive and active sensors ~~are suitable for detecting convective cloudsbeginning from their CI (Mecikalski et al., 2010). For passive sensors, a combination of data in the~~ provide valuable insights into the temporal evolution of clouds. Passive sensors, especially those measuring infrared (IR) ~~spectra can be used to understand~~ radiation, help identify cloud-top ~~signatures. While they provide a detailed view of the horizontal evolution of the cloud (Jones et al., 2023)~~features (Mecikalski et al., 2010). However, they lack ~~information on the vertical cloud structure (Haberlie and Ashley, 2018). Relying only on infrared (IR) brightness temperatures as a proxy for convective activity can lead to a misclassification of cirrus or stratiform clouds as deep convection(Kukulies et al., 2021)~~vertical resolution, making it difficult to distinguish between deep convection, stratiform clouds, and cirrus (Liu and Zipser, 2008) . In contrast, active sensors ~~provide more detailed information on the vertical dimension (Bacmeister and Stephens, 2011). Previous studies by Bacmeister and Stephens (2011) or Oreopoulos et al. (2017) used the radar reflectivity from active sensors to detect the vertical structure of hydrometeors.Nevertheless~~like radar can resolve vertical cloud structures and hydrometeor distributions (e.g., Bacmeister and Stephens (2011); Oreopoulos et al. (2017)). Still, both sensor types ~~derive data only from a 2D perspective or for a limited area. Following Masunaga and Luo (2016) , global~~ offer only limited spatial or temporal coverage. As Masunaga and Luo (2016) point out, a global, continuous 3D ~~observations could deepen the understanding~~ view of convective clouds ~~. However, no operating satellite provides this seamless coverage of the cloud structure~~remains unavailable from current satellite missions.

~~Convective cloud detection often consists of differentiating core regions from their surrounding background (Steiner et al., 1995) . A convective feature is defined by a cold peak in its core region and an associated anvil with a warmer temperature (Fiolleau and Roca, 2013 . Morphological characteristics, such as aspect ratio, length, width, and area, classify different types of convective systems (Ganetis et al., 2018). Clouds appear as moving phenomena due to diffusive, advective, dynamic, and thermodynamic processes (Sokolowsky et al., 2024). Early studies on their life-cycle often relied on manually identifying cloud movements (Masunaga and Luo, 2016 . In recent years, the development of~~ Early studies relied on manual tracking, but automated detection algorithms ~~increased the amount of processed data significantly (e.g., Fiolleau and Roca (2013); Feng et al. (2023); Heikenfeld et al. (2019))~~now enable

the processing of large datasets. Most of these algorithms ~~detect individual clouds or cloud clusters before linking the identified objects from one time step to the next (Prein et al., 2024).~~

~~Today, a variety of tools exist for cloud tracking. However, they are often limited to a specific use case. To account for the detection of convective cores and their corresponding anvil clouds, Fiolleau and Roca (2013) developed the~~ are centroid-based, linking cloud objects across time steps (Prein et al., 2024). One of the earliest and most influential tools is *TITAN* Dixon and Wiener (1993) , later adapted into *~~TOOCAN~~TINT* ~~algorithm, which works well with MCSs but shows less robust results for isolated DCCs (Sokolowsky et al., 2024). Single convective cellsundergo a more rapid dynamic development over relatively short timescales compared to MCSs (Orlanski, 1975). They are typically tracked using data from active remote sensing sensors (Haberlie and Ashley, 2018) . The pioneering work in this field is~~ Raut et al. (2021), which is optimized for tracking fast-evolving storm cells. *~~TITAN~~TOOCAN*, developed by ~~Dixon and Wiener (1993) and recently updated by Raut et al. (2021) as *TINT*. Feng et al. (2023) designed the~~ Fiolleau and Roca (2013), focuses specifically on convective cores and associated anvils in MCSs. More recently, general-purpose tools such as *PyFLEXTRKR* ~~framework to provide a more general approach to tracking any~~ (Feng et al., 2023) and *tobac* (Heikenfeld et al., 2019) have emerged. *PyFLEXTRKR* offers flexible 2D ~~atmospheric objects through time. Although it offers a high degree of flexibility, its application is limited to two spatial dimensions. Contrasting, the~~ tracking, while *tobac* ~~package allows the analysis of a~~ supports 4D ~~time series (Heikenfeld et al., 2019). Data with a higher dimensionality may offer an in-depth perspective on convective systemsand their feedback mechanisms (Prein et al., 2024; Patra and Kalapureddy, 2021)~~ analysis, enabling a more comprehensive view of convective systems.

~~Even though convective systems have been studied for decades , there is limited knowledge on~~ Despite decades of research, knowledge of the 3D ~~characteristics of DCCs. Due to~~ structure of convective cores remains limited. In the absence of ~~suitable~~ high-resolution, global 3D ~~data, the impact of DCCs on the cloud life-cycle is predominantly derived from~~ observational data, our understanding of the relationship between cores and overall cloud evolution relies heavily on 2D observations ~~or simulation data (Cui et al., 2021). While active~~ and simulations. Active and passive sensors ~~provide versatile information on the horizontal and vertical cloud structure, the sensors are subject to a spatio-temporal sampling in either dimension~~ contain important vertical or horizontal information, but are limited in their spatial and temporal coverage (active) or offer only an approximation of the vertical column (passive) (Masunaga and Luo, 2016; Taylor et al., 2017). To ~~close the data availability~~ address this gap, we ~~use~~ apply a machine learning (ML) framework to ~~extrapolate~~ reconstruct contiguous 3D radar ~~reflectivities~~ reflectivity fields from 2D ~~sensors~~ satellite data (Brüning et al., 2024). Our goal is to ~~provide a detailed perspective of the combined~~ simultaneously capture the horizontal and vertical evolution of convective clouds and their ~~DCCs. For each time step of 15 min, we predict a 3D radar reflectivity field by combining high resolution geostationary satellite imagery and the~~ cores. We use imagery from the Meteosat-11 SEVIRI sensor as input to the ML model, which is trained to reconstruct vertical cross sections ~~of a cloud profiling radar~~ based on CloudSat Cloud Profiling Radar (CPR) ~~. The data is merged into a 4D time series. Afterwards, we employ~~ observations. This approach allows us to extrapolate a continuous 3D cloud field between 2.4 and 24 km altitude. The resulting dataset combines the spatial and temporal characteristics of the SEVIRI input with the vertical structure from CPR. We then use the *tobac* package to identify convective ~~cloud trajectories within the predicted cloud field. Our aim is to compare the temporal variability of~~ clouds and track them over time in 15-minute intervals. This enables the analysis of 3D convective

cloud and core properties over ~~land and sea. A particular interest lies in assessing the cloud life-cycle for different degrees of convective organisation~~both land and ocean. A focus is comparing the life-cycles of clouds with single versus multiple core regions, offering insights into the spatial clustering and organization of convection.

We organise the article as follows. In Sect. 2, we present the data used in this study. Section 3 provides ~~an overview of the approach used for tracking and filtering convective clouds. We focus on the identification of isolated convective cells and MCSs, including the detection of DCCs~~details on details the ML-based 3D reconstruction and tracking methodology. Section 4 presents ~~a statistical analysis of~~ the results focusing on the ~~diurnal and seasonal distribution~~ temporal variability of convective cloud and core characteristics and the connection between the cores and cloud life-cycle. Section 5 ~~discusses the current limitations of the study and modifications of cloud organisation over land and sea~~compares our findings to known tropical convection characteristics and outlines limitations. Finally, Sect. 6 contains the ~~summary and principal conclusions~~concluding remarks.

2 Data

The area of interest (AOI) ~~covers a region in West Africabetween between~~ for this study spans a tropical region over central and western Africa, extending from 30° ~~N–30~~N to 30° S and 30° ~~W–30~~W to 30° E. ~~We exclude extra-tropical regions from the analysis due to their diverging convective development (Jones et al., 2024). The environmental conditions in the AOI favour~~ This region is characterised by environmental conditions that contribute to the development of ~~intense convective activity (Takahashi et al., 2023). Furthermore, its heterogeneous landscape promotes high spatio-temporal variations in the occurrence and intensity of convective activity. Clouds with high convective activity, like MCSs, still challenge forecasts and risk assessments (Jackson et al., 2022; Vondou, 2012). We use six months of data from March to August 2019 reflecting the northward shift~~ convective clouds (Takahashi et al., 2023). Our objective is to detect and analyse convective clouds and their life-cycles by a six month period between March and August 2019. This period was selected to highlight key characteristics of 3D cloud structures across different surface types within the AOI. Particular attention is given to the seasonal northward migration of the Inter-Tropical Convergence Zone (ITCZ) and the onset of the West African ~~monsoon~~ Monsoon (WAM). ~~The WAM substantially influences the West African climate and induces a high proportion of the accumulated annual rainfall , leading to frequent convective activity (Andrews et al., 2024; Kniffka et al., 2019). Our goal is to investigate the seasonality of convective clouds during the rainy season in the spring and summer, particularly regarding the impact of DCCs on the cloud life-cycle (Nicholson, 2018)~~Since the WAM plays a critical role in shaping West Africa's climate and is responsible for a significant portion of the annual rainfall in the AOI, its arrival is expected to enhance the frequency of convective cloud formation (Andrews et al., 2024; Kniffka et al., 2019).

~~For this study, we use data~~ To investigate these phenomena, we employ a ML algorithm that generates time series of 3D radar reflectivity fields based on 2D satellite observations, as described in Brüning et al. (2024). The input data are derived from the Spinning Enhanced Visible and Infrared Imager (SEVIRI) ~~sensor~~ onboard the Meteosat-11 (MSG) satellite (Schmetz et al., 2002). ~~As MSG SEVIRIis centred~~ The AOI is situated near the nadir of SEVIRI, which is positioned above the Equator

Table 1. Overview of ~~MSG~~ Meteosat SEVIRI channels (Schmetz et al., 2002).

Channel	Wavelength (µm)	Description	Spatial resolution at nadir	Retrieval at nighttime
VIS0.6	0.56-0.71	Visible channel	3 km	No
VIS0.8	0.74-0.88	Visible channel	3 km	No
NIR1.6	1.5-1.78	Near infrared window	3 km	No
IR3.9	3.48-4.36	Near infrared window	3 km	Yes
WV6.2	5.35-7.15	Upper-troposphere water vapour	3 km	Yes
WV7.3	6.85-7.85	Lower-troposphere water vapour	3 km	Yes
IR8.7	8.30-9.10	Mid infrared window	3 km	Yes
IR9.7	9.38-9.94	Ozone sensitivity	3 km	Yes
IR10.8	9.80-11.80	Clean longwave window	3 km	Yes
IR12.0	11.00-13.00	Dirty longwave window	3 km	Yes
IR 13.4	12.40-14.40	CO2 sensitivity	3 km	Yes
HRV	0.5-0.9	High-resolution visible	1 km	No

at 0° longitude~~, our AOI is close to the nadir of the sensor. It provides measurements for~~ . SEVIRI captures multispectral imagery across 12 channels in the visible, near-infrared, and thermal-infrared ~~spectra. From these , 11 have~~ ranges. Eleven of these channels offer a temporal resolution of 15 ~~min~~ minutes and a spatial resolution of 3 km~~; one is a~~ , while one high-resolution visible channel ~~with a nadir resolution of~~ provides 1 km resolution at nadir (Table 1). ~~We apply a machine learning (ML) algorithm to predict a time series of 3D radar reflectivities from 2D satellite data described in Brüning et al. (2024). The validation data for the ML model display vertical cross-sections of the cloud radar reflectivity. These data originate from the 94-GHz cloud profiling radar (CPR) onboard the CloudSat polar-orbiting satellite. The CPR is an active sensor that emits radiation pulses toward the Earth to detect vertical profiles of cloud hydrometeors (Oreopoulos et al., 2017). It has a vertical resolution of 240 m with 125 bins and a horizontal resolution of 1.4 km across and 1.8 km along the track (Stephens et al., 2008) . We train our model using radar reflectivities from the level-2 2B-GEOPROF product filtered by the cloud mask quality flag (Marchand et al., 2008).~~

To ~~extract training samples, we apply a spatio-temporal matching scheme to the satellite data (Taylor et al., 2017). The output of this routine is fed into a Res-UNet, which was designed for a seamless segmentation of images of arbitrary size (Ronneberger et al., 2015). Our studies employs the Res-UNet to predict seamless 3D cloud reflectivities with~~ validate our ML-based predictions, we use vertical cross-sections of radar reflectivity from the 94-GHz Cloud Profiling Radar (CPR) onboard the polar-orbiting CloudSat satellite. This active radar instrument transmits microwave pulses toward Earth to detect vertical profiles of cloud hydrometeors. The CPR achieves a vertical resolution of 240 m (distributed across 125 bins) and a horizontal resolution of ~~3 km . Due to CPR signal contamination at low altitudesand a lack of~~ 1.4 km across-track and 1.8 km along-track (Stephens et al., 2008). For this study, we use the level-2 2B-GEOPROF product. To address signal attenuation

at lower altitudes, we limit the vertical analysis to 90 height levels ranging from 2.4 km to 24 km (Sassen and Wang, 2008) . Additionally, due to reduced sensor sensitivity at high altitudes, the ~~predictions are prone to lack shallow convection and ice clouds (Sassen and Wang, 2008; Haynes et al., 2009). To account for the attenuation, we use only 100 height bins~~ CPR may underrepresent certain cloud types, particularly thin ice clouds like cirrus. To mitigate noise, we filter the 2B-GEOPROF dataset using the CloudSat cloud mask quality flag (Marchand et al., 2008).

3 Method

3.1 Machine learning-based reconstruction of a 3D cloud field

In the following section, we briefly outline the method used to reconstruct a 3D cloud field, based on the framework developed by Brüning et al. (2024). Our approach employs a ML algorithm built on a 2D Res-UNet architecture — a modified version of a convolutional neural network specifically designed for image segmentation tasks (Ronneberger et al., 2015). While the model is primarily trained to reconstruct vertical cross-sections of the CloudSat ~~data predicting radar reflectivities between 2.4 and 24 km height on a scale between -25 and 20 dBZ (Baemeister and Stephens, 2011). The temporal resolution of 15 min resembles the native temporal resolution of SEVIRI. While the original approach used data from 11 SEVIRI channels , we leave out channels with central wavelengths in the visible spectra to enable predictions at night time (Jones et al., 2023). Changes to the configuration for the ML model, input data and reported model error (RMSE) as described in the original paper can be found in Table 2. We detected no reduction in the modelperformance due to these modifications. Instead, the average error of~~ CPR radar reflectivity using imagery from the MSG SEVIRI satellite, its output represents full 3D radar reflectivity volumes rather than just 2D slices.

The reconstructed 3D cloud field spans an area from 60° W to 60° E and from 60° S to 60° N, corresponding to 2400 × 2400 pixels in the horizontal dimensions. SEVIRI satellite imagery serves as input to the Res-UNet model, hence the horizontal resolution of the ~~model decreases from 3.05 dBZ to~~ 3D data is 3 km x 3 km. Initially, 11 channels covering the visible, near-infrared, and thermal-infrared spectra were used (Table 1). For this study, we exclude the visible channels to ensure the model can make predictions independent of daylight conditions (Table 2).

Training data consist of 128 × 128 pixel patches of SEVIRI imagery that are spatially and temporally aligned with CloudSat overpasses. Each training sample includes a diagonal CPR cross-section. Due to the spatial resolution mismatch between MSG SEVIRI and CloudSat, we downsample the SEVIRI data to match the CPR's horizontal resolution. To address the strong class imbalance between cloudy and cloud-free conditions, we limit cloud-free samples to a maximum of 10 % of the training data. The model is trained on nine months of data and validated on a separate three-month period. The Res-UNet is trained to reconstruct CloudSat-like 3D reflectivity volumes with a horizontal size of 100 × 100 pixels and a vertical size of 90 levels. The predicted radar reflectivity values range from –25 to 20 dBZ and retain the 15-minute temporal resolution of the original SEVIRI input. We use an L1 loss function (mean absolute error) during training to evaluate the model's performance. Notably, direct validation is possible only for the diagonal cross-section, which accounts for about 10 % of each training sample. For the three-month test period, the modified daylight-independent model achieves a root mean square error (RMSE) of 2.99 dBZ

Table 2. Modifications to the Res-UNet applied in this study originally proposed in Brüning et al. (2024)

Parameter	Original configuration	Modification
Number of input channels	11	8
Loss function	L2	L1
Nighttime predictions	No	Yes
Average RMSE	3.05	2.99

~~. The reported error~~ — an improvement over the original model (Table 2). This level of accuracy is comparable to ~~a precision of~~ the 5 dBZ ~~achieved by~~ precision reported for other CloudSat products (Tomkins et al., 2024). ~~We leverage the predicted data to detect and track convective clouds. Compared to methods based only on ground-based or active radar, the ML-based model can provide enhanced coverageof the contiguous~~

To generate complete coverage of the domain between 60° W to 60° E and 60° S to 60° N, the individual 3D output patches are stitched together, producing a unified output volume of with a size $2400 \times 2400 \times 90$ pixels. This method may help to obtain a consistent spatial coverage, particularly over remote oceanic regions where active sensors are sparse (Prein et al., 2024). Visual inspection confirms the absence of artifacts at tile boundaries, indicating a seamless reconstruction of the 3D cloud field ~~, especially over remote oceanic regions(Prein et al., 2024). We merge the~~ in different parts of the domain. To further assess model performance, we compute cloud top heights (CTH) from the predicted radar reflectivity and compare them to CTH values from the CMSAF CLAAS-V002E1 dataset (Finkensieper et al., 2020). The comparison reveals that the model captures realistic spatial patterns of CTH in both tropical and mid-latitude regions. However, model accuracy tends to decline with increasing distance from the MSG SEVIRI nadir. Finally, the time-series of 3D radar ~~reflectivities along their temporal dimension to create~~ reflectivity volumes is merged along the temporal axis to generate a 4D ~~time series used for further analysis~~cloud field, which is used to detect and track convective clouds. For the purposes of this study, we crop the domain to consist of 1200×1200 pixels, covering the region between 30° W–30° E and 30° N–30° S — effectively focusing on the area between the Tropic of Cancer and the Tropic of Capricorn.

4 ~~Method~~

3.1 Tracking convective clouds in 4D

In this study, we analyse the ~~spatio-temporal evolution~~ development and properties of convective clouds by employing the *tobac* package~~(Heikenfeld et al., 2019). It is~~ , a modular Python-based package for tracking atmospheric objects in ~~a~~ 4D time series ~~(Prein et al., 2024)~~(Heikenfeld et al., 2019). In this study, we use the recently released version 1.5 of the software package (Sokolowsky et al., 2024). ~~It preserves the contiguity of the data in the horizontal and vertical dimensions, allowing an enhanced analysis of meteorological characteristics in 3D.~~ We merge the predicted ~~radar reflectivity~~ 3D radar reflectivity fields along the

temporal dimension and feed the 4D time series into the tracking algorithm to create continuous trajectories. The workflow to identify possibly convective trajectories consists of three steps: detecting cloud features by their centroid's position, segmenting the associated cloud field for each centroid, and linking segmented objects through time (Figure 1, ~~a-c). We separate elongated cloud clusters if they~~ a–c). Moreover, we aim to separate cloud clusters that are only connected by a few pixels in the horizontal and vertical dimensions ~~to avoid incorrect label assignments (Oreopoulos et al., 2017). This workflow~~ (Oreopoulos et al., 2017) . The workflow of this object-based approach is depicted in Fig. 1 and will be explained in the following paragraphs.

The framework, while enabling detailed analysis of convective cores, has limitations. The predicted 3D cloud fields represent model-based approximations rather than direct observations, reflecting patterns learned by the ML model. Additionally, using fixed thresholds in the object-based detection may oversimplify complex structures associated to clouds in the atmosphere. Nonetheless, we may employ the data to enable a large-scale, high-resolution tracking of convective systems over the tropical Atlantic and continental Africa.

3.1.1 Identifying cloud features

~~This study aims to reconstruct the cloud life-cycle from CI to the dissipation phase (Section 1). Although the radar~~ Radar reflectivity does not directly measure vertical ~~velocity, it can be used as a proxy for convective intensity (Luo et al., 2008) . For the cloud detection, we use~~ air velocity, but it can serve as a valuable proxy for detecting hydrometeors associated with convective cloud development (Luo et al., 2008). To identify potential cloud structures, we apply a fixed threshold of ~~-15 dBZ to differentiate signals from potential clouds and background noise within the radar reflectivities (Marchand et al., 2008) . The threshold is weakly restrictive and might lead to the integration~~ –15 dBZ to distinguish signals of hydrometeors from background noise in the radar reflectivity data (Marchand et al., 2008). While this threshold is only moderately restrictive — allowing for the inclusion of short-lived ~~features in the results (Sokolowsky et al., 2024). Nevertheless, we keep this threshold to detect and track the~~ or weak features — it is intentionally chosen to capture the full spatio-temporal evolution of convective clouds ~~from CI to dissipation (Esmaili et al., 2016). At first,~~ between development and dissipation stage (Esmaili et al., 2016).

The detection process begins by applying a Gaussian filter with a sigma ~~filter size~~ value of 0.5 ~~smoothes~~ to smooth the input data ~~(Kukulies et al., 2021). Afterwards, contiguous regions are labelled, applying the same threshold of -15 dBZ (Figure 1, a). The centroid of each feature is determined by the weighted mean of its position along three spatial dimensions (Heikenfeld et al., 2019). All centroids are~~ and reduce noise (Kukulies et al., 2021). We then compute the centroid of each potential cloud using a weighted center-of-mass approach. Here, each point's weight is defined by its reflectivity value above the –15 dBZ threshold (Heikenfeld et al., 2019). These centroid positions are each assigned a unique identifier~~that is kept during the following steps. Following, we use a watershed segmentation~~ , which is maintained throughout the subsequent tracking and segmentation steps.

Next, we apply a 3D watershed segmentation algorithm to delineate the ~~3D cloud field associated to~~ spatial extent of individual cloud structures associated with each centroid. ~~The approachoriginates from geology and is used in image segmentation tasks. Here, the input data are treated~~ In this approach, the 3D radar reflectivity field is interpreted as a topographic ~~map divided into individual catchments along adjacent~~ surface, where higher reflectivity values represent peaks and surrounding areas are

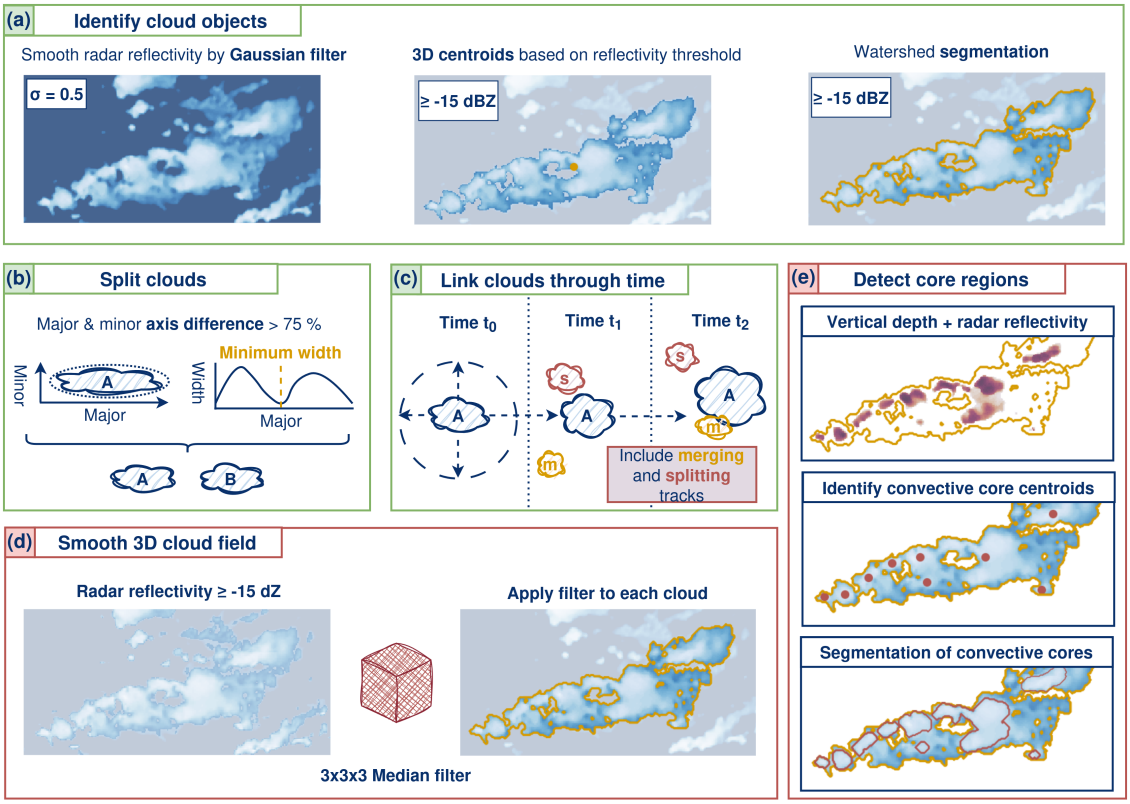

Figure 1. Workflow for tracking convective clouds **(a)**–**(c)** and their convective cores **(d)**–**(e)** using an object-based algorithm and ML-based 4D radar reflectivities. The routine consists of **(a)** the identification and segmentation of convective cloud ~~features~~ centroids and volumes using a radar reflectivity threshold ~~of –15~~ of -15 dBZ, **(b)** splitting ~~elongated features~~ shallow connected objects along their major axis, and **(c)** linking the labelled cloud ~~features~~ objects through time. For detecting ~~DCCs, we apply a fixed threshold of -15 dBZ. In (d)~~cores, we apply a Median filter with a kernel size of 3x3x3 pixels to ~~each~~ smooth the 3D radar reflectivities associated to each cloud ~~field~~label **(d)**. ~~Following, the approach includes~~ We aim to identify convective core regions by adding **(e)** ~~calculating~~ the number of ~~contiguous~~ pixels ≥ higher than 0 dBZ ~~for~~ and the average cloud radar reflectivity in each vertical cloud column~~and adding~~ . This step provides a 2D layer of the ~~cloud top~~ combined radar reflectivity and potential core depth, which is used to ~~identify centroids~~ search for local maxima displaying the centroid locations of ~~DCCs and to~~ convective cores. Subsequently, we apply a watershed segmentation to algorithm to derive the ~~associated area for each~~ core area.

segmented like catchment basins divided by ridges (Meyer, 1994). We ~~feed the 3D radar reflectivity image with~~ initialize the algorithm by placing markers at the detected centroids ~~into the watershed algorithm to delineate the pixels associated with each centroid (Jones et al., 2023). The value of each pixel is decreased towards its local minimum using a threshold of -15 dBZ~~ in a binary 3D volume, where all other grid points are set to zero. From each marker, the algorithm expands through the volume, assigning reflectivity-based pixels to the corresponding cloud until the threshold of –15 dBZ is reached. The result is a ~~labelled cloud maskfor each time step (Fiolleau and Roca, 2013). In a 3D cloud field, the number of~~ labeled 3D cloud mask, where each voxel is either zero (indicating no cloud) or an integer label corresponding to a specific cloud object (Fiolleau and Roca, 2013) . This mask allows us to quantify the volumetric structure of clouds: the total number of labeled pixels per centroid ~~represents the cloud~~corresponds to the cloud's volume rather than ~~the cloud area(Sokolowsky et al., 2024). In response, we calculate the aggregated~~ its area. For analyses requiring horizontal cloud coverage, we compute the 2D ~~cloud anvil area using~~ projected area by taking the column-wise maximum ~~for further analysis (Table 3)~~across vertical levels.

3.1.2 Split shallow connected clouds

After identifying the cloud centroids and ~~associated cloud area~~their associated areas, we analyse the morphology of each ~~object. The goal is to separate elongated objects connected only at the location of the local minimum width of the cloud anvil~~ cloud object to determine whether it may represent a merger of multiple cloud systems (Figure 1, b). To ~~detect these minima, we derive the~~ do this, we examine the labeled cloud mask to locate local minima in the cloud area, which may indicate potential split points between merged cloud structures. The shape of each cloud is characterised using the best-fitting ~~ellipse for each cloud (Ganetis et al., 2018). Then, we calculate the ratio between the major and minor cloud axes~~ellipse (Ganetis et al., 2018) . We then calculate the aspect ratio — i.e., the ratio of the major to minor axis lengths. If the ~~difference between the axes is higher~~ major axis is more than 75 % ~~, we consider the cloud~~ longer than the minor axis, we classify the cloud as elongated (Cui et al., 2021). The ~~coordinates~~ orientation of the major axis ~~give us~~ provides the direction of elongation~~. Then, we determine the location of the split by analyzing~~ , which guides the search for potential split locations. Next, we examine the aggregated 2D cloud area ~~and the change points of the area distribution . We~~ along this direction and analyse the area distribution to detect change points. If the distribution is unimodal — featuring a single peak — we perform no split. However, if the distribution is ~~unimodal with a single maximum. Otherwise, we split the cloud if~~ multimodal, we apply a split at the local minimum~~diverges~~ , provided that this minimum deviates by more than 75 % from the mean size of the cloud shield~~(Figure 1, b). We~~ . Then, we update the segmentation results by assigning ~~an~~ a unique label to ~~the separated objects~~each newly separated cloud object.

3.1.3 Spatio-temporal linking

~~We link the~~ We track 3D ~~objects through time~~ cloud objects over time by linking them based on their ~~movement speed (Heikenfeld et al., 2019). In contrast to a 2D linking routine, the~~ estimated movement speed, following the method of Heikenfeld et al. (2019 . The 3D perspective ~~enables an in-depth~~ allows for detailed analysis of both ~~the~~ horizontal and vertical ~~evolution, which is crucial for assessing the growth of DCCs (Fiolleau and Roca, 2013). For~~ cloud evolution—an essential aspect for understanding core development. At each 15-minute ~~time step~~interval, we predict the ~~movement of the objects based on their velocity~~

in the expected location of a cloud object using its velocity from previous time steps (Figure 11, c). We reduce the time needed for the search processby defining a maximum spatial radius between two consecutive To streamline the linking process, we define a maximum search radius between time steps. Within this radius , potential links are identified and clouds are connected (Kukulies et al., 2021). Emerging clouds are assigned Only cloud objects within this radius are considered potential matches, significantly reducing computational effort. When new clouds form, we assign them the average velocity of clouds in their neighbourhood nearby clouds to estimate their likely movement (Sokolowsky et al., 2024). Due to limited computational resources, we only computational limitations, we apply the linking for algorithm to only two consecutive time steps simultaneously. A temporal overlap of 15 minutes and a contiguous identifier determine whether to merge tracks. Afterwards, we check the cloud anvil area at a time. We assume a successful link is established when a cloud object maintains a 15-minute temporal overlap and shares a consistent identifier across steps. For instance, we compare the cloud areas of linked objectsto avoid false assignments. For that purpose, we apply a minimum area similarity of at least 50 % (Prein et al., 2024) . Depending on the features' previous and subsequent movements, we estimate two objects to merge together or split off and include this , assuming that genuinely connected trajectories may exhibit more similar area changes than unrelated clouds (Prein et al., 2024). Finally, we evaluate the movement patterns before and after each time step to infer whether cloud objects may be merging or splitting and include the information in the derived final cloud trajectories.

3.2 Detect convective core regions

After linking the trajectories, we apply a second detection algorithm to identify DCCs with a strong vertical ascent within the cloud's lower regions (Zipser and LeMone, 1980). A convective cloud typically contains Convective clouds often contain one or more of these updraft regionswith heavy rainfall that translates through core regions, which are typically associated with stronger updrafts and intense precipitation that can penetrate above the freezing level(Igel et al., 2014). The growth and decay of DCCs in these regions is particularly interesting for the intensity of convective clouds (Takahashi et al., 2017). In our study, we employ the ML-based radar reflectivity to identify the number and size of DCCs for each labelled cloud (Figure 1, d,e). We note that the radar reflectivity cannot replace a calculation of the vertical velocity. However, it provides information on the distribution of hydrometeors beneficial to estimate convective activity (Yuter et al., 2005; Luo et al., 2008). We mask reflectivitiesbelow -15 dBZ to detect convective core regions (Bacmeister and Stephens, 2011). Then, we apply a Median filter with a kernel size of 3x3x3 pixels to smooth . Because the formation and dissipation of these cores are closely linked to severe weather events, analysing their behavior is of particular interest (Takahashi et al., 2017).

To detect convective cores, we use the previously generated labelled 3D cloud mask (Section 3.1.1), derived from the ML–based radar reflectivity data. There are different approaches to identify convective cores from radar reflectivities. These methods may comprise the detection of convective precipitation, which may be associated to core regions in hydrometeors (Haynes et al., 2009; Pilewskie and L'Ecuyer, 2022) or the analysis of the radar reflectivity (Tomkins et al., 2024). In our employing fixed thresholds along the vertical column (Luo et al., 2008; Bacmeister and Stephens, 2011; Igel et al., 2014). In this study, we identify a DCC in the focus on combining the latter with an object-based detection algorithm to identify centroids of convective cores in the predicted 3D cloud fieldby a combined maximum of the column-wise aggregated radar reflectivity

field. The approach is applied to each labelled cloud for each time step along the cloud trajectory (Figure 1, d,e). We begin by smoothing the radar reflectivity data associated with each cloud label using a 3×3×3 median filter. Core centroids are identified by locating local maxima in a combined metric that incorporates both smoothed radar reflectivity and the ~~difference between the cloud top height (CTH) and cloud base height (CBH) for a vertically contiguous cloud layer(cloud vertical depth) (Takahashi et al., 2017).~~

~~As visualised in Fig. 1e, we start with~~ vertical extent of a contiguous potential core layer. Specifically, we calculate the mean radar reflectivity for each vertical cloud column, then determine the height of this core layer by counting the number of pixels ~~≥~~ with reflectivity values higher than 0 dBZ ~~in each cloud column to estimate the cloud vertical depth (Tomkins et al., 2024). We expand~~ located at more than 5 km height. In our study, we do not include cores occurring lower than cloud base layer, where our model predictions may be less robust. We aim to fill isolated gaps for otherwise vertical continuous cores by expanding the threshold from ~~≥~~ 0 dBZ to ~~≥ 5 dBZ if~~ 5 dBZ in columns that contain at least one pixel ~~passes the first criterion (Igel et al., 2014). The cloud column is discarded if the CBH is ≥~~ higher than 0 dBZ (Igel et al., 2014; Luo et al., 2008). We apply a minimum vertical extent of 5 km ~~or if the vertical profile shows no convective pixels for more than 50 % of the CTH (Masunaga and Luo, 2016). Otherwise, we add the mean radar reflectivity of the vertical profile to the derived vertical depthof the column (Oreopoulos et al., 2017). We~~ for a column to be considered part of a core; otherwise, its value is set to zero. The approach is visualised in Figure 1 (e). We add both indicators (average reflectivity and potential core vertical depth) for each pixel associated to a cloud label, resulting in a 2D layer in which we search for local maxima ~~of the combined cloud vertical depth and radar reflectivity to identify centroidsof potential DCCs. Then, we mask the DCC area by a watershed segmentation. In case we find no maxima, the number of cores is set to zero (Feng et al., 2023)~~to serve as candidate core centroids. ~~For all clouds with at least one DCC, we calculate the number of cores, core area, core vertical depth, and core lifetime (Table 3). For more than one DCC, we additionally derive the mean distance between DCCs (Bacmeister and Stephens, 2011)~~If no local maxima are found - e.g., in case no columns contain pixels higher than 0 dBZ at more than 5 km height - the cloud is recorded as having zero cores for that time step (Feng et al., 2023). When one or more core centroids are identified, we use a 3D watershed segmentation to delineate the core volumes. This process is repeated for every cloud object at each time step throughout its life-cycle, whereas a cloud may contain multiple cores at the same time.

3.3 Extract cloud and core properties

~~For each trajectory along space and time for an individual detected object~~ For each detected cloud trajectory, we extract both horizontal and vertical characteristics to describe the cloud and its internal structure (Table 3). Cloud properties include cloud area, CTH, CBH, duration, eccentricity, and the ~~associated cloud and core properties as displayed in Table 3. While some of these properties can be derived from 2D data by analysing peaks in e.g., the IR spectra of geostationary satellites, approximating the vertical column is often error-prone, e.g., when cirrus at the cloud top layer are mistaken for deep convection. For instance, ground-based radar receive 3D data which can be used to assess the cloud vertical structure. However, they deliver only few information about clouds developing over remote oceanic regions. Most passive and active sensors lack the data coverage to enable a seamless analysis of~~ ratio of core to total cloud area. The cloud lifetime displays the total lifetime of the trajectory in

hours, beginning from the first detection. Cloud area is calculated from the column-wise maximum of the 3D cloud mask, while vertical (CTH, CBH) metrics come from the number of pixels in the ~~3D convective cloud structure over different surface types. Our approach allows for a more holistic perspective on cloud development over land and sea. We may derive horizontal cloud properties, like the anvil area or cloud eccentricity, and vertically resolved properties, like the CTH, simultaneously (Table 3) . Furthermore, analysing the structure of DCCs by our 3D data may deepen the insights on convective activity in convective core regions. We employ the radar reflectivity at a fixed altitude of 10 km as a measure of convective activity. The ratio between the major and minor cloud axes are used to calculate the eccentricity which describes the best fitting ellipse for the cloud . Values range between 0–1, with higher values~~ vertical column associated to each cloud label. Eccentricity is derived from the best-fitting ellipse, with values closer to 1 indicating a more ~~spherical~~ circular shape (Cui et al., 2021). ~~For convective clouds, the eccentricity may affect its hazard potential (Gallus et al., 2008). For example, linear convective systems are more prone to heavy wind and precipitation (Semie and Bony, 2020). Additionally~~We also record the cloud's travel distance and assign a surface type using a binary land-sea mask and the modal value for the locations of the cloud trajectory within this land-sea mask. The ratio of core to cloud area may provide a measure of convective compactness and intensity (Haberlie and Ashley, 2018) . For clouds with one or more cores, we calculate the ~~ratio between the area of the convective core and cloud anvil as a measure of convective strength and compactness (Haberlie and Ashley, 2018)~~number, mean area, height, lifetime, eccentricity, and average distance between cores. The core area and height are derived from the column-wise maximum horizontal extent and vertical extent of the previously identified cores, , similar to the cloud area and CTH. These metrics may help characterise the structural properties of detected cloud systems.

~~We divide the life-cycle of convective clouds in three phases and assess~~

3.4 Filter convective cloud trajectories

We filter the cloud trajectories to exclude possibly non-convective tracks from the analysis (Figure 2). For that purpose, we require the cloud tracks to have at least one core and a radar reflectivity of higher than 0 dBZ at 10 km height for at least 15 min along the trajectory. Additionally, we apply a minimum CTH of 10 km and a maximum CBH of lower than 5 km for the cloud during at least one time step (Igel et al., 2014; Luo et al., 2008). While we do not require the convective clouds to have a CTH higher than 10 km at every time step during their trajectory, we discard the trajectories that never reach the CTH threshold. The criteria may help to identify convective clouds with an evolved cloud base and vertical height that may be typically associated to tropical convection (Li et al. (2021), Takahashi et al. (2023)).

3.5 Investigating the cloud life-cycle

We analyse the temporal evolution of detected clouds to explore how variations in the cloud life-cycle relate to the number of convective cores. For this purpose, we divide each cloud's life-cycle into three idealised stages, following the framework proposed by Futyan and Genio (2007). Each stage corresponds to distinct spatio-temporal changes ~~of the cloud properties as shown in Fig. 2~~in cloud structure, as simplified illustrated in Figure 3. The first time step of ~~the trajectory defines~~ each trajectory marks the beginning of the ~~convective initiation (CI) (Futyan and Genio, 2007). For each point in time, we calculate~~

Table 3. Features used to describe the ~~morphology, physical~~ properties ~~,~~ and life-cycle ~~transition~~ statistics of detected convective clouds and cores.

Feature type	Feature name	Definition
Cloud	Cloud area	Area of the cloud ~~anvil~~ (km²)
	Cloud top height (CTH)	Maximum height of the cloud (km)
	Cloud base height (CBH)	Minimum height of the cloud (km)
	Area ratio	Ratio between cloud ~~anvil area & DCC~~ area & core area
	Eccentricity	Roundness of the best fitting ellipse (cloud)
	Reflectivity	Average radar reflectivity of the cloud at 10 km height (dBZ)
	Location	Longitude and latitude of the cloud centroid (°)
	Travel distance	Euclidean distance for coordinates at initiation and dissipation (°)
	Cloud lifetime	Lifetime of the cloud trajectory (h)
	Surface type	~~Value of the~~ Modal value from a binary land-sea mask for the cloud trajectory
Core	Number of cores	Number of identified convective core regions
	Core ~~size~~ area	Average ~~size~~ area of convective cores (km²)
	Core vertical depth	Depth of the ~~DCC~~ core in the vertical column (km)
	Mean distance	Average distance between ~~DCCs~~ cores in a cloud cluster (km)
	Core lifetime	Average lifetime of the ~~DCCs~~ cores (h)
	Core eccentricity	Roundness of the best fitting ellipse (core)
Life-cycle	~~Cooling~~ Reflectivity gradient	Reflectivity change rate at 10 km height (dBZ)
	Area growth	Relative cloud area expansion (%)
	Vertical growth	Vertical growth of the cloud (km)

~~the difference between the~~ development stage. Unlike methods that assess cloud stages using a cooling induced by temperature changes, the ML-based radar reflectivity does not provide information on temperatures. As an alternative, we approximate the life-cycle using temporal changes in radar reflectivity at 10 km height ~~at CI and the current time step to approximate the cooling of the convective cloud . Furthermore, the 3D data allows us to simultaneously derive~~ and the resulting vertical and horizontal cloud characteristics. For estimating the vertical growth of the cloud~~. It describes~~ , we compute the difference between ~~the CBH and CTH at CI for each time step, compared to CI. The highest difference of the radar reflectivity displays the maximum cooling and induces a transition between the CI and the maturity phase (MAT) (Takahashi et al., 2023). During the MAT,~~ CTH and CBH (i.e., to display the height of the cloud layer) for every point in time. For the horizontal growth of the cloud~~anvil increases. The end of the MAT is marked when the cloud anvil reaches its maximum relative size compared to the anvil size at CI. We further track the cloud until dissipation and we detect no more cloud centroid $\geq$ -15 dBZ (Crook et al., 2019).~~ , we calculate changes of the cloud area derived as proportional differences to the cloud area at the first timestep of detection.

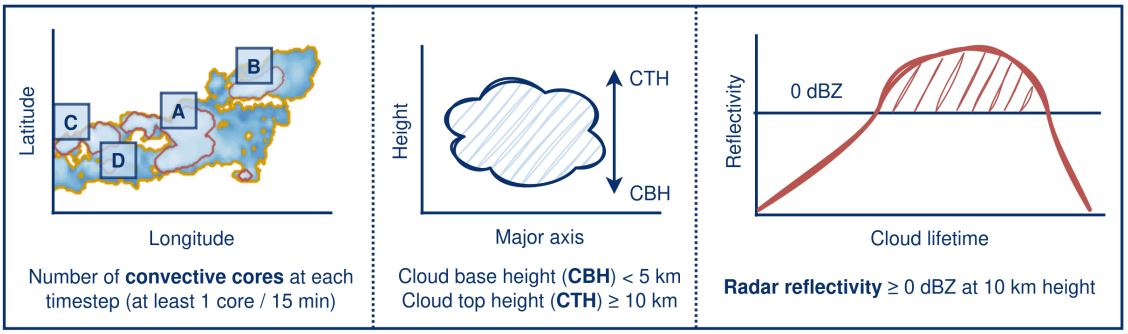

Figure 2. Criteria for filtering potentially convective cloud trajectories. The criteria consist of counting the number of convective cores (A–D) for each labelled cloud along the cloud lifetime. Moreover, we check the cloud base height (CBH) and cloud top height (CTH) of the cloud, and the radar reflectivity at 10 km height along the cloud trajectory. Following, we estimate the trajectory to belong to a convective cloud if we detect at least one core, a CBH lower than 5 km, a CTH higher 5 km, and a radar reflectivity higher than 0 dBZ at 10 km height for at least 15 minutes along the cloud lifetime.

- *Development stage*: Building on the approach by Luo et al. (2008), we use a radar reflectivity threshold of 0 dBZ at 10 km altitude as a proxy for potential cloud-top cooling, which may be indicative of convective growth. We calculate the temporal gradient of radar reflectivity at 10 km for each cloud trajectory, identifying the time of maximum increase to mark the cloud development stage. This stage may be associated with a high cloud vertical layer and strong updrafts that support continued vertical growth (e.g., Kikuchi and Suzuki (2019); Chen et al. (2021)).The transition from development to maturity is defined by the time of maximum radar reflectivity increase (Takahashi et al., 2023; Hu et al., 2021).

- *Maturity stage*: Following the time of maximum radar reflectivity, the reflectivity gradient at 10 km height may gradually decrease. Instead, both the vertical thickness and horizontal extent of the cloud typically may increase in the maturity stage, indicating a sustained growth of the cloud (Gupta et al., 2024).

- *Dissipation stage*: Dissipation begins when vertical growth slows and the cloud reaches its maximum horizontal size. We continue tracking the cloud until the reflectivity falls below the −15 dBZ threshold and no centroids are identified during feature detection, indicating cloud decay (Crook et al., 2019).

For each trajectory, we ~~derive the point in time where transitions occur between~~ determine key time points that may approximate changes in the cloud life-cycle~~phases (maximum cooling, maximum anvil~~ : the moment of maximum reflectivity gradient at 10 km, peak area (horizontal) growth, maximum vertical ~~growth, dissipation). Additionally, we determine the point in time with~~ extent, and the onset of dissipation (Table 3). We also record when the highest number of ~~DCCs and maximum DCC size to compare statistics for isolated and clustered clouds .~~

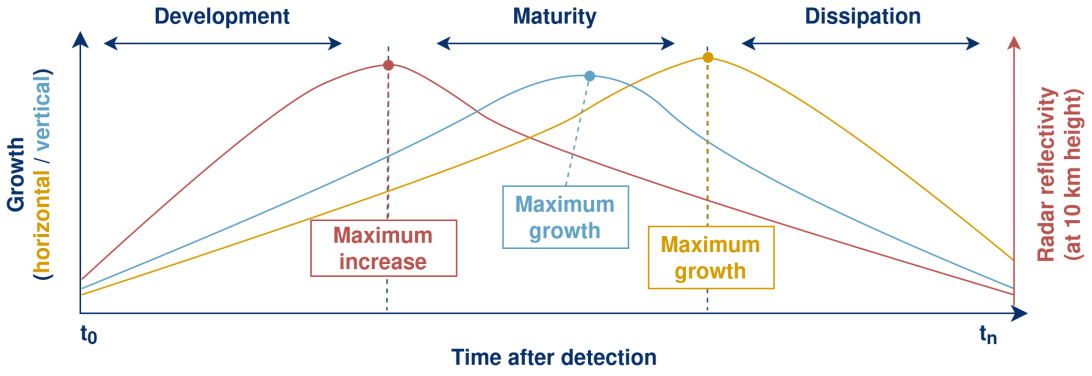

Figure 3. ~~Criteria for filtering convective clouds from the derived trajectories. These consist of counting the number of convective cores (A-D) for each cloud whereas we require minimum~~ Schematic visualisation of ≥ ~~1 DCC to pass as a convective cloud. We check~~ the ~~cloud base height~~ three stages (~~CBH)~~ development, maturity, and ~~cloud top height (CTH~~dissipation) of the ~~cloud~~idealised convective life-cycle. Here, ~~and~~ we show how changes of the radar reflectivity at 10 km height~~along~~, the horizontal growth of the cloud ~~trajectory~~area, and the vertical growth of the cloud vertical layer may be connected to the transition between life-cycle stages.

~~Schematic visualisation of the three stages of the convective life-cycle. We show the changes of the cloud anvil areal and the radar reflectivity at 10 km that induce a transition between convective initiation (CI), maturity (MAT), and dissipation. Additionally, we include the vertical growth of convective clouds derived from the 3D radar reflectivites.~~

3.6 ~~Filter convective cloud trajectories~~

~~We filter the trajectories based on morphological and microphysical cloud properties (Section 3.2) to exclude non-convective tracks from the analysis (Figure 3~~cores is detected and when cores reach their maximum area. These markers are used to compare life-cycle characteristics between clouds with a single core and convective systems containing multiple cores (i.e., more than one core). We ~~select all tracks that show at least one DCC and a reflectivity peak of ≥ 0 dBZ at 10 km height for at least 15 min along the trajectory (Igel et al., 2014). Additionally, we apply a minimum CTH of 10 km to account for the typical convective properties within the tropics (Li et al., 2021). A maximum CBH of ≤ 5 km is used to discard clouds without an evolved cloud base (Bacmeister and Stephens (2011),Takahashi et al. (2023))~~note that the life-cycle statistics derived for this study are based on the ML-based radar reflectivities and inherit the uncertainties connected to these predictions. Hence, they may only provide an approximation of distinct changes occurring within the cloud trajectories over time.

4 Results

4.1 ~~Evaluation~~ Distribution of convective cloud ~~trajectories~~and core properties

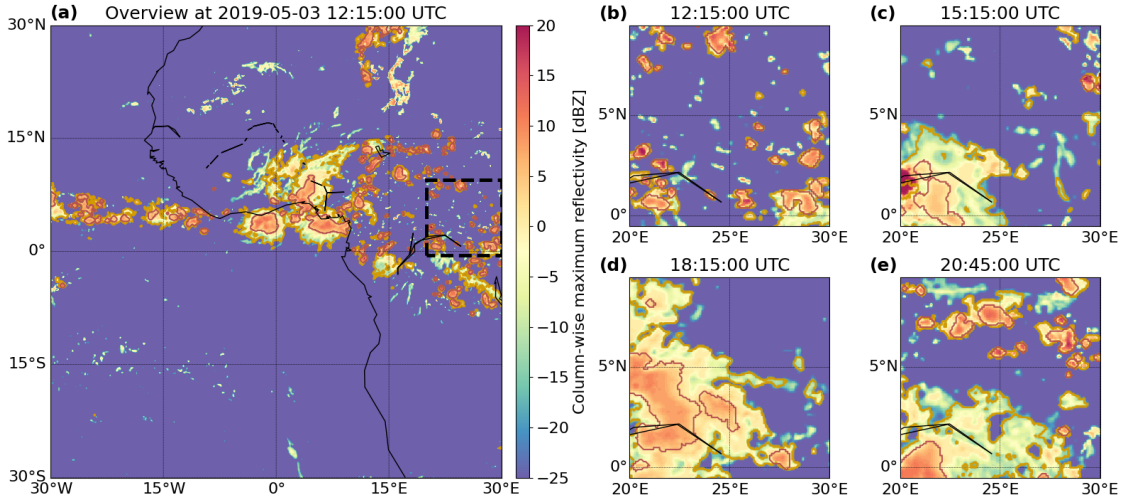

Figure 4. An example of convective clouds (orange outline) and their cores (red outline) detected ~~by~~ in the ~~tracking approach for~~ ML-based 3D cloud field on the 03.05.2019, 12:15:00 UTC. The cloud mask is plotted over the 3D radar reflectivity~~aggregated by~~ , which shows the aggregated column-wise maximum. All times are given in UTC. In **(a)**, we see an overview of the AOI, **(b)** to **(e)** show a zoomed perspective in 3 h intervals (black square).

~~From March to~~ Between March and August 2019, we ~~detect~~ detected approximately 375,000 convective clouds using ML-based 3D radar reflectivity data. After excluding tracks with a lifetime of only one timestep, 338,142 cloud trajectories remained for analysis. Figure 4 shows an example ~~of the tracked DCCs and their associated anvils. We observe a high number of convective clouds~~ from May 3, 2019, at 12:15 UTC, highlighting tracked convective clouds and cores. While regions over Morocco and Mauritania showed radar reflectivity higher than 0 dBZ, no vertically continuous convective systems were identified there. Instead, numerous convective clouds appeared over the Gulf of Guinea, the equatorial rainforest, and the Atlantic Ocean. ~~As seen over Morocco and Mauretania, a high radar reflectivity at the cloud top does not necessarily indicate the presence of a deep convective system (Kukulies et al., 2021). In Fig. 4b–4 e, we zoom in to observe the evolution of the cloud systems in 3-hourly intervals. Our findings show that DCCs often persist only for~~ Figures 4 (b)–(e) illustrate the development and dissipation of cores, often lasting only a short time. ~~Furthermore, we may find several DCCs within MCSs at the same time which indicates a higher convective activity in the cloud cluster compared to the presence of a single DCC~~ Some clusters contained multiple cores, potentially indicating mesoscale convective systems (MCSs) (Takahashi et al., 2017).

~~We extract the 3D properties not only for the cloud anvil but also for each DCC.~~ Our 3D ~~perspective allows to track the cloud's~~ framework allows us to simultaneously track horizontal and vertical ~~development simultaneously (Takahashi et al., 2023) . To derive statisticsfor the DCCs~~cloud development. For core statistics, we separate the core region from the anvil cloud, as ~~visualised in Fig. 5.~~

~~An example of the convective clouds (orange outline) and their cores (red outline) detected by the tracking approach for the 03.05.2019 12:15:00 UTC. The cloud mask is plotted over the 3D radar reflectivity aggregated by its cloud top maximum. In~~

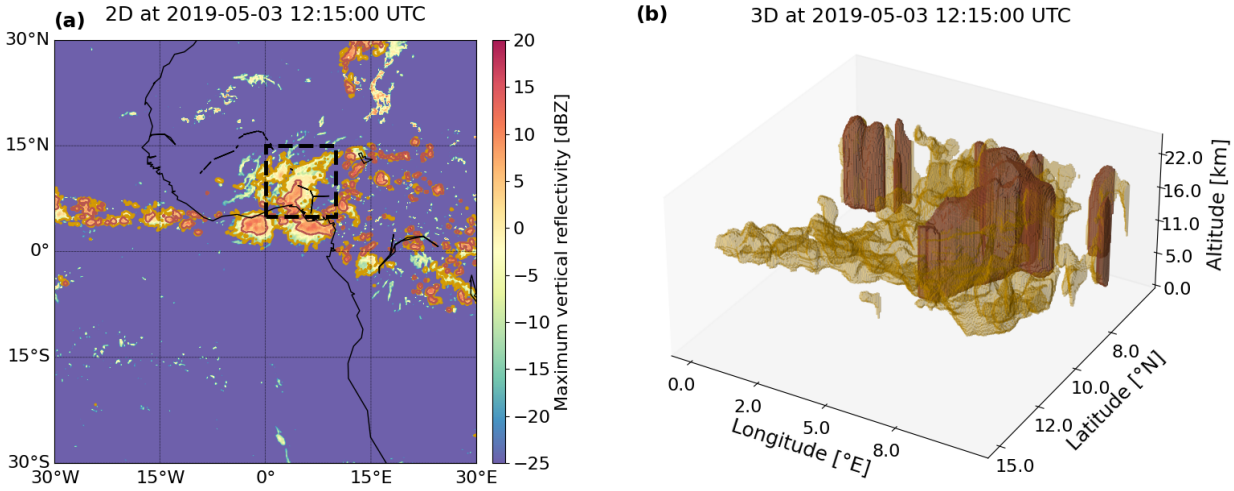

Figure 5. An example of the convective clouds (orange outline) and their cores (red outline) detected in the predicted 3D cloud field on the 03.05.2019, 12:15:00 UTC. The cloud mask is plotted over the 3D radar reflectivity, which shows the aggregated column-wise maximum. In **(a)**, we see an overview of the AOI, **(b)** shows the zoomed perspective (black square) in 3D for the cloud volume (orange) and core volume (red).

~~**(a)**, we see an overview of the AOI, **(b)** shows the zoomed perspective (black square) in 3D for the cloud volume (orange) and core volume (red).~~

~~We group the detected clouds based on the number of associated DCCs to differentiate isolated clouds with a single DCC~~ and ~~clustered systems with multiple DCCs (Li et al., 2021). Clouds~~ shown in Figure 5. Clouds are grouped by core count to distinguish potentially more isolated systems (one core) from clustered systems (multiple cores). For statistical purposes, clouds with 6–9 cores and those with ~~ten~~ 10 or more cores are ~~grouped for the statistical analysis (Jones et al., 2024). Most of our trajectories (80 %) contain clouds with a single core (~~combined into respective categories (Jones et al., 2024).

Single-core clouds make up roughly 65 % of all trajectories (Figure 6, a)~~. The proportion considerably declines with an increasing number of DCCs. Clouds with ten or more DCCs account for about 10 % of all trajectories. Figure 6b shows the lifetime grouped in 3-hourly intervals. Deep convection generally appears on a wide range of scales, whereas most clouds are short-lived, with a lifetime of up to 3 h. For higher lifetimes, the proportion of trajectories steadily decreases. The distribution of the surface type is analysed in Fig. 6c. About 70 % of our tracks are located over sea and 30~~ , with the frequency decreasing as core count increases. Only about 5 % of clouds have 10 or more cores. Most clouds (80 %) have lifespans between 0–6 hours (Figure 6, b). Surface type distribution reveals that 65 % of clouds form over the ocean and 35 % over land~~. Compared to the actual land surface distribution, we observe a shift of about 5–10 % towards the sea as convective systems in tropical Africa propagate towards the Atlantic Ocean. The difference between single- and~~ —about a 10 % shift toward ocean compared to

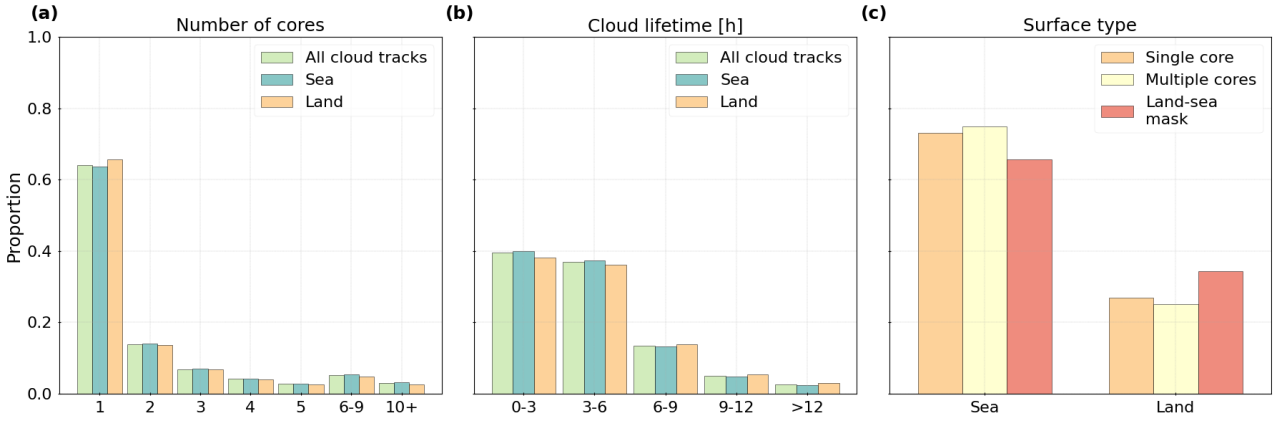

Figure 6. ~~Cloud statistics for~~ Distribution of **(a)** the number of associated cores, **(b)** the average cloud lifetime~~on a logarithmic scale~~, and **(c)** the ~~distribution of the~~ surface type derived from a land-sea mask compared to the ~~location at CI~~ modal locations of detected clouds with a single core or multiple cores. We show the distribution in **(a)** and **(b)** for ~~single-~~ all cloud tracks (~~1 DCC~~n = 338,142)~~and multi-core~~ , clouds over the ocean (~~> 1 DCC~~n = 249,484), and clouds over land (n = 88,658).

land-sea coverage (Figure 6, c). Among single-core clouds, 70 % occur over the ocean, while for multi-core clouds~~accounts for up to 5 %over each surface type. We observe slightly more isolated cells over continental Africa and more clustered systems over the Atlantic Ocean. This finding emphasises we may find more favourable conditions for the development of intense convective clusters over the ocean~~ , the figure is 75 %. This imbalance — 249,484 oceanic clouds vs. 88,658 continental — may reflect differences in tropical landmass distribution and the eastward propagation of convective systems. Oceans may also offer more favorable conditions for multi-core development (Cui et al., 2021).

We ~~analyse the distribution of~~ assess how the 3D cloud ~~physical properties for different numbers of DCCs (Table 3). For isolated clouds with a single DCC, we observe a substantially shorter lifetime and travel distance than for clusters with several DCCs, particularly for clusters with more than 10 DCCs~~ properties described in Table 3 may vary with core count and surface type. Our findings show that single-core clouds have shorter lifetimes and travel distances than multi-core systems (Figure 7, a–b). ~~In contrast, the cloud eccentricity is less dependent on the number of DCCs (Figure 7,e). For~~ Eccentricity exhibits a weak variation across all groups, ~~we see an eccentricity~~ mostly ranging between 0.6–0.7 ~~, with only a singular peak at 0.8 for single-core clouds. The cloud anvil area varies considerably stronger between each DCC group than the roundness of the clouds. Most single-core clouds have an anvil area $\geq$ 1000 km^2. The area increases with the number of DCCs~~(Figure 7, c). Cloud area increases significantly with core count, especially for clouds with ~~more than~~ 10 ~~DCCs~~ and more cores (Figure 7, d). ~~For instance, the anvil size and CTH are~~ CTH is 10–20 % ~~higher over the landthan sea. The~~ greater over land, yet radar reflectivity at 10 km height ~~increases with the number of cores, in particular for highly clustered systems~~ and cloud area are slightly higher over the ocean (Figure 7, d–f). CTH increases from 15.5 km for single-core clouds to 17.25 km for multi-core ones (Figure 7, ~~e). It is on average 0.5 dBZ higher over the ocean than over land. Overall, differences in the intensity of convection are~~

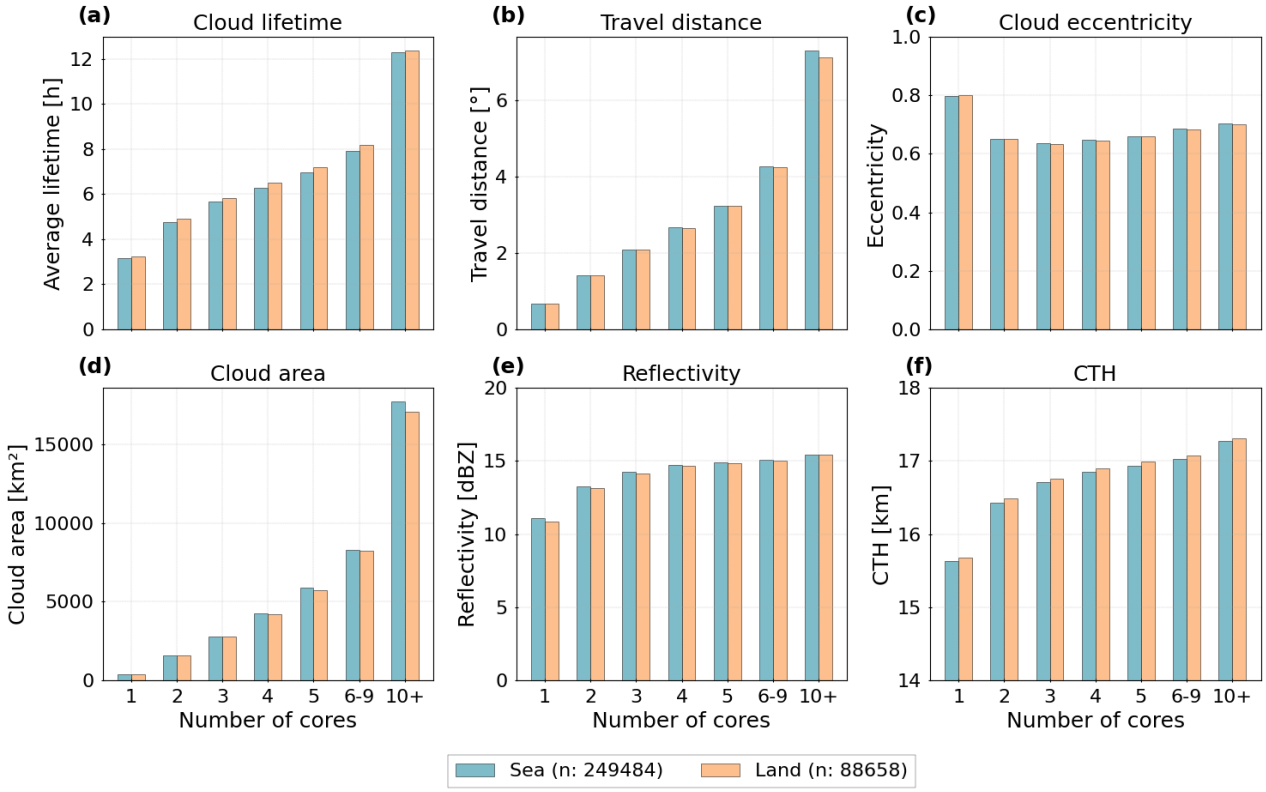

Figure 7. ~~Cloud~~ Distribution of cloud statistics grouped by the number of associated cores for **(a)** the cloud lifetime, **(b)** the travel distance ~~from CI to dissipation~~between first and last detection, **(c)** the cloud eccentricity, **(d)** the cloud ~~anvil~~ area, **(e)** the radar reflectivity at 10 km height, and **(f)** the CTH.

~~higher between isolated and clustered clouds than for different surface types~~f). Land–sea differences are more pronounced for single-core clouds. Despite expectations based on previous tropical studies (Deng et al., 2016; Takahashi et al., 2017), oceanic clouds often show stronger reflectivity and larger areas — though overall surface-related differences remain small. The lower number of land-based clouds may exaggerate statistical noise.

~~Moreover, our approach allows us to simultaneously investigate the core properties for isolated and clustered clouds. Figure 8a shows the average core lifetime between initiation and dissipation. Long-lasting clouds are connected a longer core lifetime. For single-core clouds, the core persists on average for~~ The analysis of core properties (Figure 8) shows average core lifetimes of 0.3–0.4 ~~h. The core lifetime and eccentricity increase according to the cloud lifetime in Fig. 8 to 1.2 h for clustered clouds . More and long-lasting cores come along a higher vertical depth (Figure 7, d). Over the sea,~~ hours for single-core clouds, increasing to about 0.8 hours for clouds with more than 10 cores (Figure 8, a). Core eccentricity shows little variability and ranges from 0.5–0.6 (Figure 8, b). Core area is slightly larger for single-core clouds than for those with 2–9 cores but increases

considerably for clouds with 10 and more cores. For single-core clouds, we detect a larger core area over the ocean, while cores for multi-core clouds are larger over land (Figure 8, c). Core height and distance between cores ~~are more extensive for less clustered clouds . In contrast, the core size over land increases stronger with many cores . This growth is induced by drier surface conditions and a higher lifting condensation level over land , promoting a stronger convective updraft (Takahashi et al., 2017). As the core area grows, the distance between the cores increases, especially for convective clouds over land~~ both increase with core count (Figure 8, d–e). The largest distances, which may indicate the least compact core morphology, occur for clouds with 10 and more cores (Figure 8, e). The ~~ratio between the core and anvil area depends on the number of DCCs and the surface type. Overall, it is higher over the ocean (Figure~~ area ratio between clouds and cores is highest for single-core clouds and declines with more cores. The sharp decrease may be connected to a faster increase of the cloud area compared to core area for multi-core clouds (Figure 7, d, Figure 8, f). ~~For clouds with $\geq$ 2 DCCs, the ratio lies at 10 % or less, while we observe a ratio of 25 % for single-core clouds . An enhanced convective activity comes along with a lower area ratio, indicating alarger anvil outflow compared to the DCC size (Horner and Gryspeerdt, 2023). The core properties indicate on average a stronger convective activity over continental Africa, in particular when comparing highly clustered cloud systems.~~

In summary, clouds with more cores exhibit longer lifetimes, larger areas, greater heights, and increased core size and distances between cores. Core properties are broadly consistent across surface types, except for core area and core distances (Figures 7a, 8c). However, these findings may be influenced by the land–sea imbalance in our dataset and inter-annual variability.

4.2 Temporal characteristics of convective clouds

We observe a higher proportion of cloud tracks between March to May, and notably less tracks between June to August. Over land, we find more clouds in March and April. Over the ocean, the proportion of cloud tracks is higher between May and August (Figure 9, a). For the diurnal distribution, we observe slightly more tracks between 12:00 to 18:00 UTC than at other time intervals. During nighttime (21:00–06:00 UTC), more cloud tracks occur over the ocean. In contrast, we detect a higher proportion of cloud occurrences over land during the day. However, the variability connected to the diurnal cycle and surface type remain weak (Figure 9, b).

4.3 ~~Temporal characteristics of tropical convection~~

4.2.1 Diurnal cycle over land and sea

We ~~compare~~ analyse the diurnal cycle of cloud properties for single-core and multi-core clouds over ~~sea and land . Figure 9 shows the cloud lifetime , the cloud anvil area , and the~~ land and ocean by computing a 2D density distribution displaying hourly changes of the cloud properties. Figure 10 illustrates these variations in cloud lifetime (a–d), cloud area (e–h), and radar reflectivity at 10 km height ~~. For isolated clouds over land, we see a peak for the~~ (i–l). Over land, single-core clouds show an afternoon peak (12:00–16:00 UTC) in both radar reflectivity and ~~the cloud anvil areabeginning in the early afternoon (Figure 9, f, j). Continental clouds have a larger anvil area and lower reflectivity compared to clouds over the ocean. This deviation~~

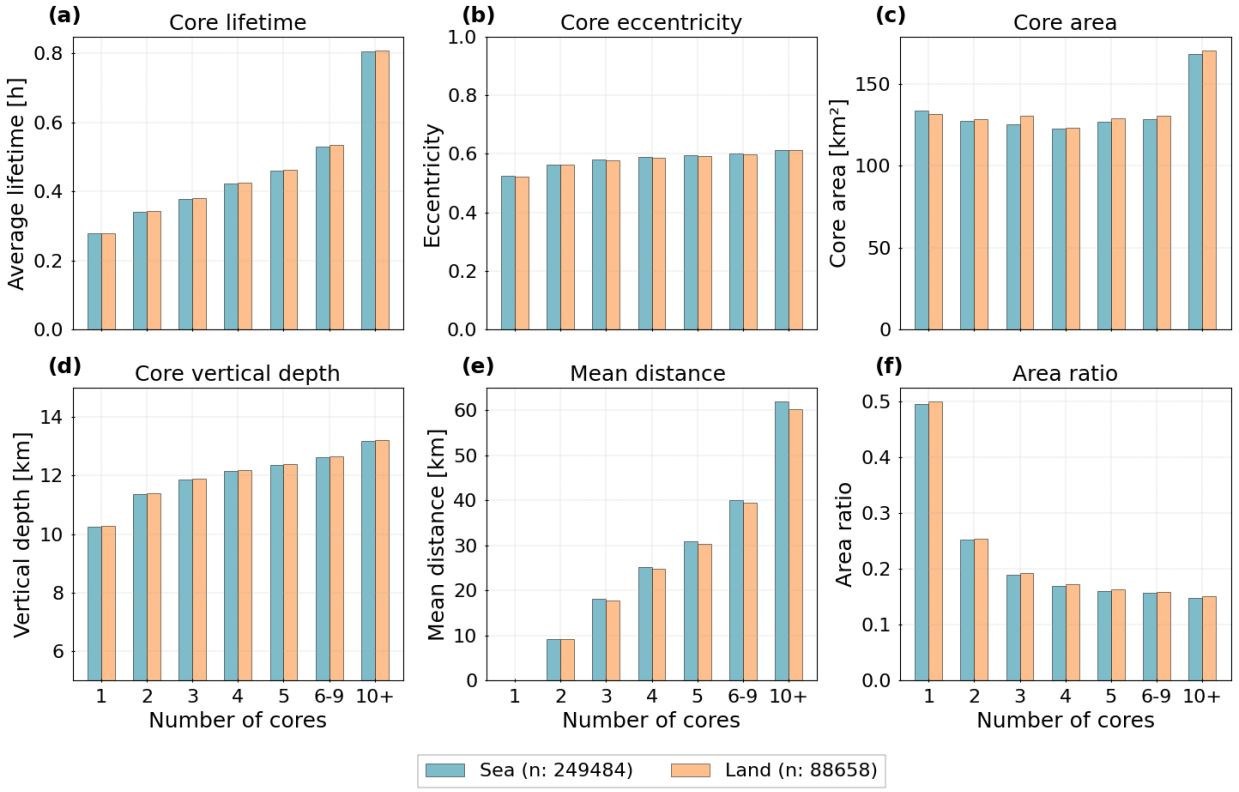

Figure 8. Distribution of core statistics grouped by the number of associated cores for **(a)** the core lifetime, **(b)** the core eccentricity, **(c)** the core area, **(d)** the vertical depth of the core, **(e)** the mean distance between individual cores, and **(f)** the area ratio between the cloud and the core.

~~may originate an enhanced local thermal instability (Cui et al., 2021). During the afternoon, environmental conditions favour the initiation of convection over land. In contrast, a more steady sea surface temperature is responsible for convective clouds developing over the ocean. Although the distribution shows a bimodal diurnal cycle with two pronounced peaks in the night and late afternoon, the formation of DCCs over the sea can occur at any time of day due to their linkage to external forcing like cold pools (Chen and Houze, 1997). Between midnight and early morning, a pronounced cooling over land reverses the land-ocean circulation. The radiative cooling at the cloud top destabilizes the boundary layer and promotes the development of oceanic convection. After sunrise, incoming solar radiation at the cloud top increases the stability and depresses the development of convection. With aweakened land breeze in the morning hours, the nocturnal convective clusters over the ocean dissipate (Houze Jr., 2004). We observe this diurnal pattern for isolated clouds, in particular. Clustered clouds have a substantially larger anvil area and higher reflectivity at 10 km height (Figure 9, g, h, k,l). Although the diurnal cycle is similar for clouds with multiple DCCs, the diurnal variability of the~~ cloud area, while cloud lifetime displays two peaks: one at night and one in the

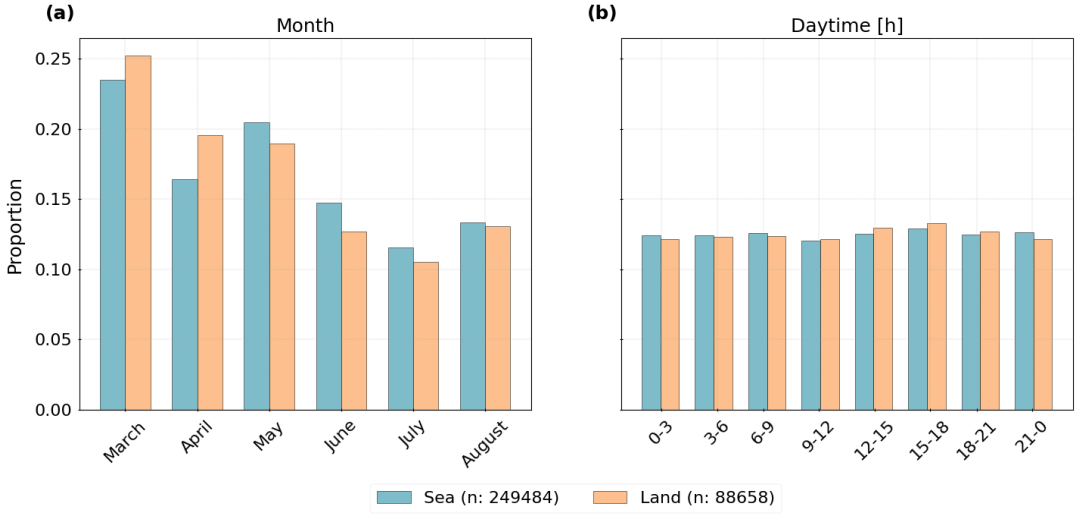

Figure 9. ~~Core statistics grouped by the number~~ Distribution of ~~associated cores~~ cloud tracks over land and sea for **(a)** the ~~core lifetime, **(b)** the core eccentricity, **(c)** the core area, **(d)** the vertical depth of the core, **(e)** the mean distance~~ months between ~~individual cores~~March–August, and ~~**(f)** the area ratio between~~ **(b)** the ~~cloud anvil and~~ daytime of the ~~core~~first detection.

morning (Figure 10, b, d). Over the ocean, the diurnal cycle is weaker or less distinct. Cloud lifetime lacks a clear diurnal peak (Figure 10, a, c), whereas cloud area and reflectivity ~~is smaller than for isolated clouds. Isolated clouds have a higher eccentricity than clustered clouds(Figure 9,a–d). Especially during peak times over sea and land , we observe an enhanced axes ratio of up to 0.9. For both surface types, an increasing number of DCCs induces a temporal shift of the afternoon peak within the radar reflectivities and the anvil area (Figure 9, k–l~~show nocturnal and daytime peaks (Figure 10, e, i, k). Despite similar diurnal patterns for the cloud lifetime and radar reflectivity, multi-core clouds consistently exhibit higher mean values than single-core clouds. These differences may reflect environmental contrasts between land and ocean. As suggested by Cui et al. (2021), local circulations over land in the tropics often trigger afternoon convection, producing the observed peaks in Figure 10 (f), (h), and (j). In contrast, more constant ocean temperatures may suppress strong diurnal variations (Figure 10, a, c, g).

~~We use our data to estimate not only horizontally resolved cloud properties, but to also extract the 3D properties of the DCCs. The diurnal pattern resembles~~ The diurnal patterns of core properties (Figure 11) largely mirror those of the cloud properties. ~~The core size, core lifetime, and core eccentricity show a bimodal distribution over the sea and a singular afternoon peak over land (Figure 10, a–l). An increased number of DCCs comes with larger cores and an enhanced lifetime , particularly for clouds over land. For clustered cloudsover land, we see a second maximum at night, which typically appears over sea surfaces. However, the afternoon peak is consistently more powerful (Figure 10, c–d~~Over land, core area peaks between 12:00–18:00 UTC for both single- and multi-core clouds. Over the ocean, single-core clouds show two peaks between 00:00–06:00 and 14:00–20:00 UTC (Figure 11, a–d). The core lifetime follows a similar pattern for single-core clouds. For multi-core clouds,

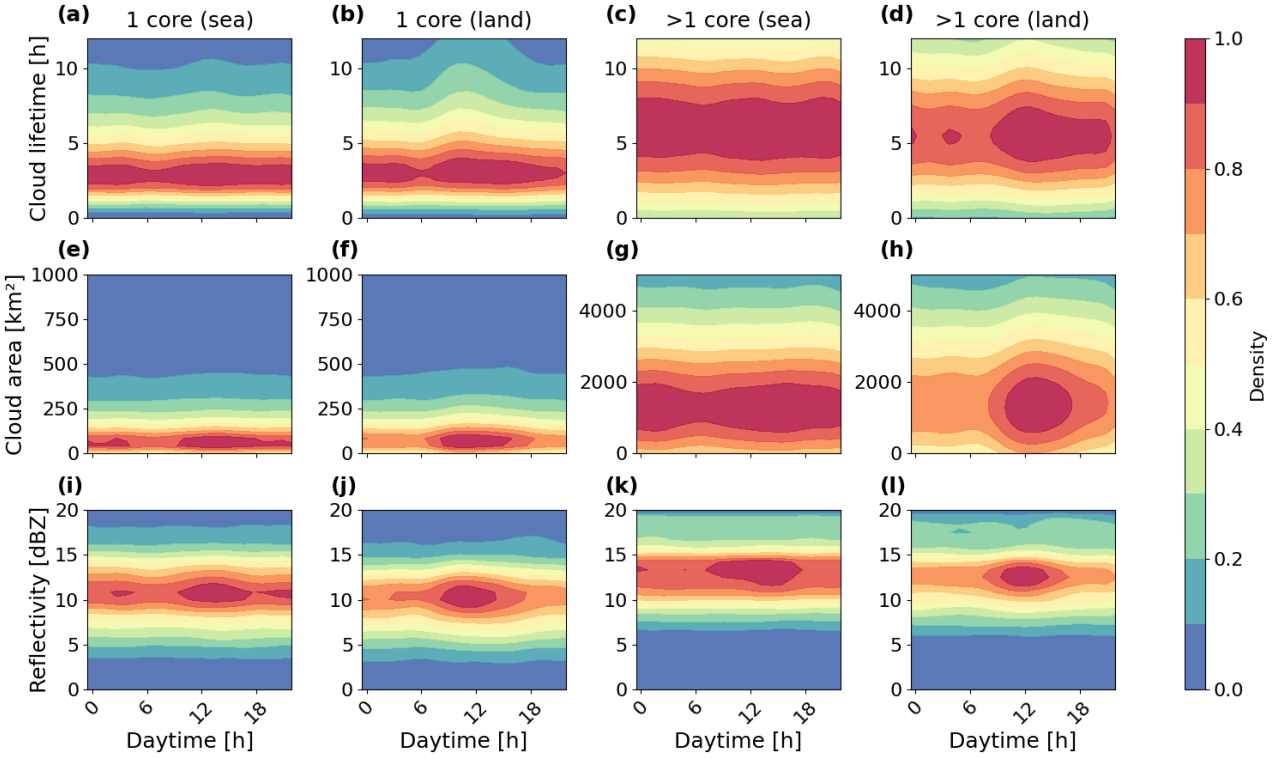

Figure 10. Diurnal cycle for cloud properties grouped by the number of associated cores and surface type. We display the hourly changes (in UTC) regarding **(a)–(d)** the cloud lifetime, **(e)–(h)** the cloud ~~anvil~~ area, and **(i)–(l)** the radar reflectivity at 10 km height for single- (1 ~~DCC~~core) and multi-core (~~>1 DCC~~more than one core) clouds over sea and land. The values show the density distribution ~~of each parameter~~ normalized between 0 and 1.

cores over land show two peaks, while oceanic cores point out no clear diurnal variation for multi-core clouds (Figure 11, e–h). For single-core clouds, peaks of the core lifetime resemble the core area (Figure 11, a, e). The ~~core eccentricity of isolated clouds shows a higher variability and a lower mean than for clustered clouds (Figure 10, i–l). The core and anvil area ratio shows a comparable primary peak between 0–0.1 for all types. Single-core cloudshave a secondary peak at 0.5, pointing out the simultaneous existence of clouds with different shapes and life-cycle phases (Figure 10,~~ distribution of the core height follows those of the core area (Figure 11, m–p). ~~Cores are more extensive and persistent over land~~ On average, clouds with multiple cores have higher and more variable values for core area, lifetime, and height. In contrast, the area ratio is lower and has a weaker variability for multi-core systems. For single-core clouds, ~~reflecting the contrast between convective intensity~~ we observe an afternoon peak over land and nocturnal and afternoon peaks over the ocean. Multi-core clouds show a weak diurnal variation, particularly over the ocean (Figure 11, i–l).

Overall, the diurnal cycle highlights a pronounced afternoon peak over land and a two peak, at nighttime and in the afternoon, over the ocean. These patterns align with observed differences in tropical convective behavior over land and sea (Vondou, 2012).

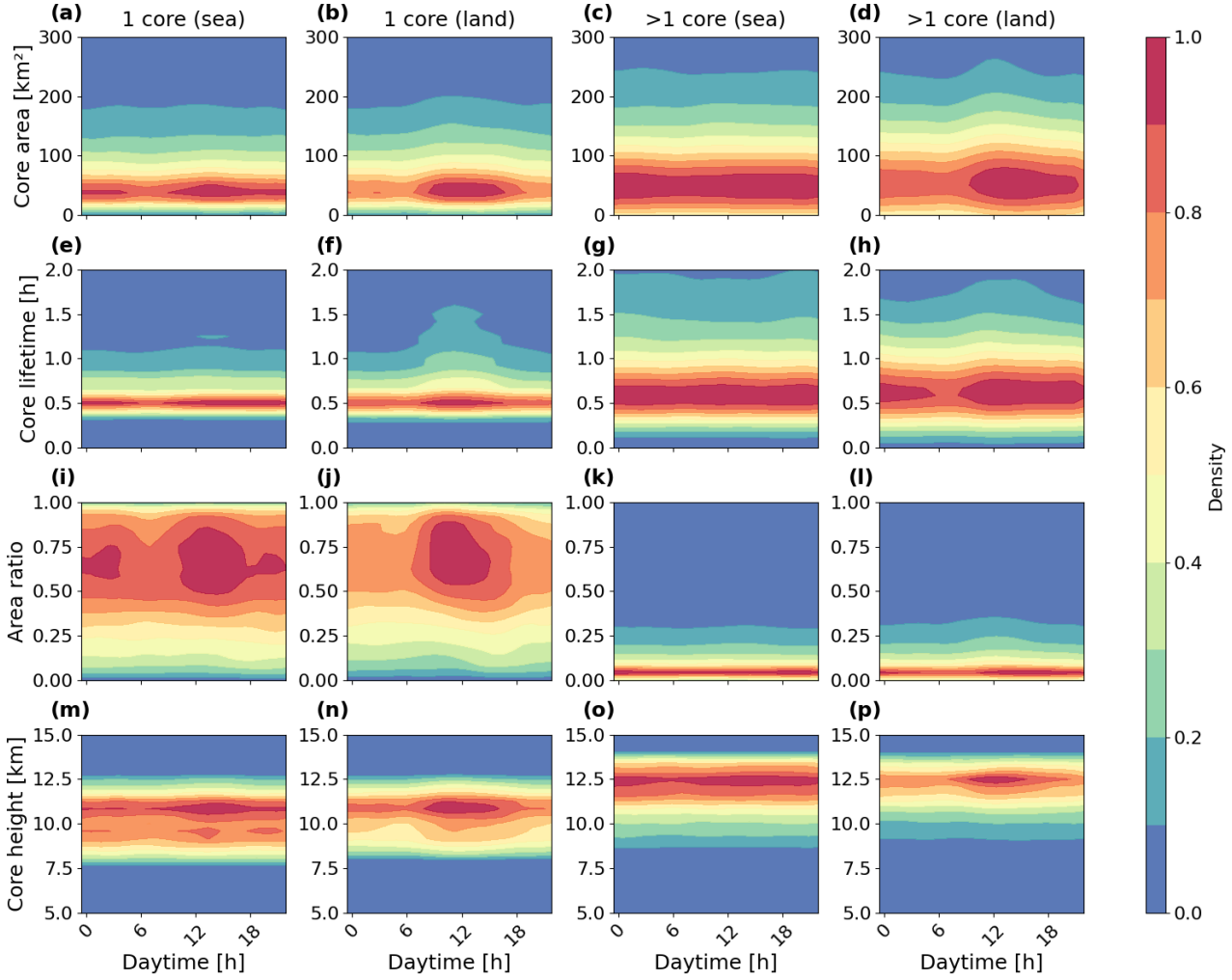

Figure 11. Diurnal cycle for core properties grouped by the number of associated cores and surface type. We display the hourly changes (in UTC) regarding **(a)–(d)** the core ~~size~~area, **(e)–(h)** the core lifetime, **(i)–(l)** the core eccentricity, and **(m)-(p)** the area ratio between the cloud core and anvil area for single- (1 ~~DCC~~core) and multi-core (~~>1 DCC~~more than one core) clouds over sea and land. The values show the density distribution ~~of each parameter~~ normalized between 0 and 1.

While we find those patterns mostly for single-core clouds, results for multi-core clouds — especially over the ocean - are less distinct.

4.2.2 ~~Seasonal~~ Monthly variability of convective ~~clustering~~properties

~~Within the tropics, the seasonal cycle of atmospheric processes substantially affects convective cloud and core development (Andrews et al., 2024). In Fig. 11, we calculate the monthly average and a rolling mean for a 7-day window for~~ For different

months, the value variability may considerably influence the development of convective clouds and their core structures within the tropics (Andrews et al., 2024). We explore these changes in Figure 12 by comparing monthly averages of the cloud area, ~~the CTH, the number of DCCs per cluster, the core size, core lifetime, and the area ratio between cores and cloud anvils. Overall, convective activity increases in summer by about 5–10 %. An enhanced core size and a decreased area ratio between cores and anvils accompany an increased average cloud anvil area. At the same time, the number of DCCs increases~~ CTH, cloud lifetime, number of cores, core area, and area ratio over land and sea for single-core and multi-core clouds.

From March to August, the cloud area shows a gradual increase for single- and multi-core cloud systems over the ocean~~and decreases over the land~~. For clouds over land, the cloud area slightly decreases (Figure 12, a). In contrast, CTH generally decreases, though month-to-month fluctuations appear to be higher than a consistent decrease (Figure 12, b). Cloud lifetime shows a higher variability between months with increases in April for single- and multi-core clouds and in April and June for single-core clouds. Overall, clouds with multiple cores exhibit a slight decline in lifetime over land. ~~The CTH shows~~ Over the ocean, lifetime rises from March to April, decreases in May, and increases again in June — returning to near-initial values by August (Figure 12, c). The number of cores per cloud increases over the ocean from March to July, followed by a sharp drop in August. Initially higher over land, core counts shift in favor of oceanic clouds after April. Convective systems over land show a ~~bimodal distribution with peaks in May and July. We observe a higher CTH, cloud lifetime , and area ratio over landthroughout the depicted time series. The differences between land and sea are less distinct regarding the number of DCCs, their size, and the cloud area.~~

~~Seasonal variability of cloud and core statistics between March and August grouped by the surface type for **(a)** the cloud anvil area, **(b)** the CTH, **(c)** the cloud lifetime, **(d)** the number of DCCs, **(e)** the core size, and **(f)** the area ratio between the cloud anvil and the core. We show the monthly mean (solid lines) and 7-day rolling mean (dashed lines) for the time series for single- and multi-core clouds over land and sea.~~

~~In Fig. 12, we compare the differences for the cloud and core properties over sea and land. For that purpose, we average the data on a monthly basis. The results are displayed in 3-hourly intervals. For most parameters, we observe that direction changes occur on a seasonal basis. The diurnal variability show less distinct patterns than the seasonal changes. Continental clouds have more extensive anvils and a higher CTH and cloud lifetime~~ decrease of core numbers from March to June, a peak in July, and another decline in August (Figure 12, ~~a–c). However, oceanic clouds become larger than clouds over land in summer (JJA)~~ d). The core area steadily increases over the ocean but fluctuates more over land (Figure 12, ~~a). Overall, the DCC properties show a higher seasonal dependency. In spring, continental clouds come with more DCCs, larger cores, and a lower area ratio than cloud over the ocean~~ e). The area ratio shows a slight decrease for multi-core clouds throughout the period, while remaining higher for single-core clouds. We observe a high monthly variability over land and ocean, whereas the area ratio remains to be higher over continental Africa (Figure 12, ~~d–f). In summer, the pattern reverses. This finding suggests that clouds appear more clustered over land in spring~~ f).

To quantify the effect of these changes, we compare average values across two periods: March–May (MAM) and ~~the ocean in summer~~ June–August (JJA). Metrics include the cloud area, CTH, cloud lifetime, number of cores, core area, and area ratio (Table 4). We calculate Cohen's D to measure effect sizes, with thresholds defined as small (< 0.2), medium (0.2–0.5), and

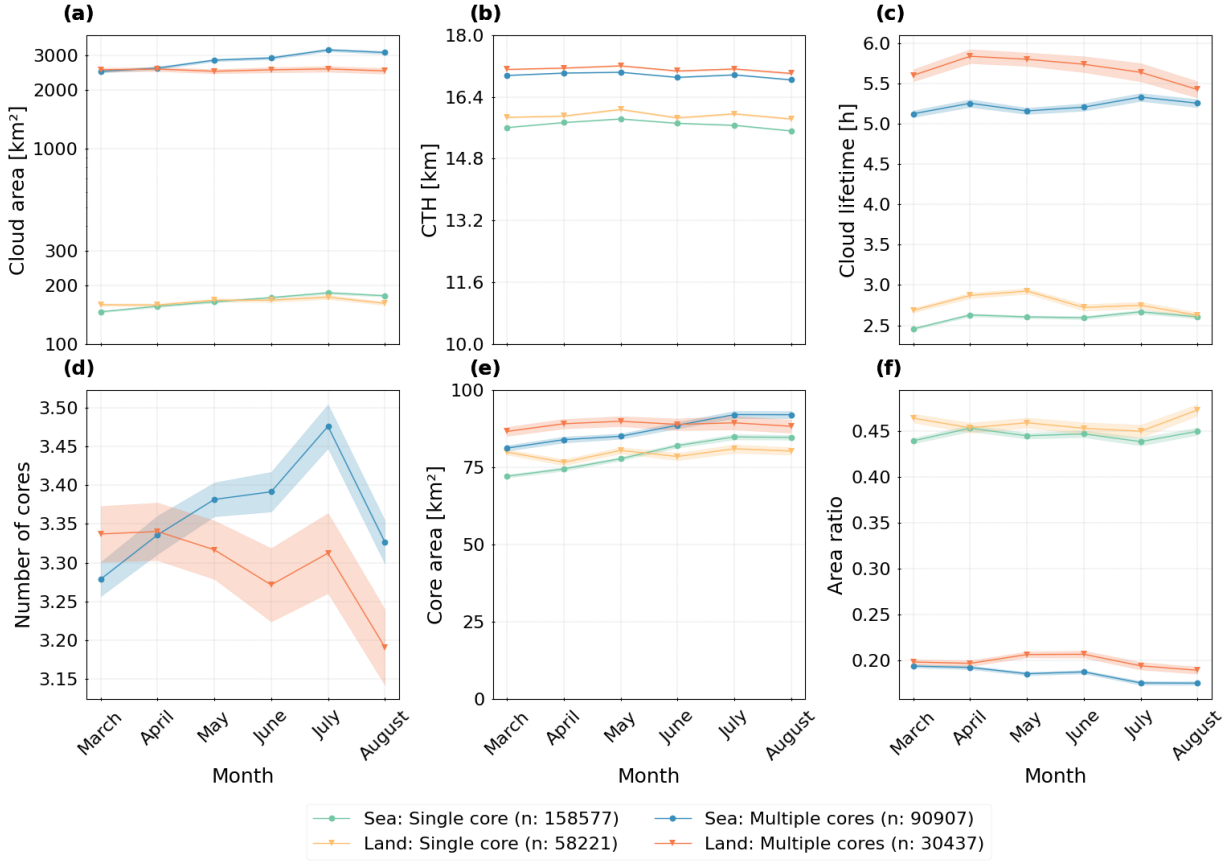

Figure 12. Monthly variability of cloud and core statistics between March and August for single-core and multi-core clouds grouped by the surface type for **(a)** the cloud area, **(b)** the CTH, **(c)** the cloud lifetime, **(d)** the number of cores (only multi-core clouds), **(e)** the core area, and **(f)** the area ratio between the cloud and the core. Line plots show the mean value with a confidence interval of 95 %.

large (> 0.8) (Cohen, 2013). Over the ocean, cloud area, number of cores, and core area are higher in JJA, while CTH, cloud lifetime, and area ratio are greater in MAM. A similar pattern emerges over land, except cloud area and number of cores are higher in MAM. Overall, observed differences between the two seasons and over land and sea remain weak. Most effect sizes are small, indicating high internal variability rather than distinct temporal trends within the period. These results highlight the importance of analysing longer time periods to account for the inherent variability and imbalance between cloud tracks over land and sea (Figures 4 and 9), which may influence the representativeness of the findings.

~~Differences between oceanic and continental cloud and core properties. Data is averaged on a monthly basis between March and August and grouped in 3-hourly intervals for **(a)** the cloud anvil area, **(b)** the CTH, **(c)** the cloud lifetime, **(d)** the number of DCCs, **(e)** the core size, and **(f)** the area ratio between the cloud anvil and the core.~~

Table 4. Comparison of mean values for cloud (cloud area, CTH, cloud lifetime) and core (number of cores, core area, area ratio) properties between March–May (MAM) and June–August (JJA) grouped by the surface type (Sea, Land). We calculate the effect size measured by Cohen's D to assess the difference between distributions over sea and land.

	March–May			June–August		
	Sea	Land	Cohen's D	Sea	Land	Cohen's D
Cloud area	1605.673	1742.597	0.017	2634.334	1681.849	0.107
CTH	16.061	16.229	0.145	15.982	16.147	0.138
Cloud lifetime	4.327	4.900	0.01	4.356	4.231	0.003
Number of cores	2.128	2.166	0.009	2.459	2.062	0.136
Core area	125.118	128.249	0.013	143.647	131.638	0.035
Area ratio	0.398	0.408	0.032	0.374	0.407	0.115

4.3 ~~The influence of DCCs on the cloud life-cycle~~

4.3 Impact of convective cores on the cloud life-cycle

~~We use the criteria defined in Sect. 3.2 to assess the transition between the three~~

4.3.1 Relationship between life-cycle statistics and cloud properties

To analyse the cloud life-cycle ~~phases dividing each cloud into a growing, a mature, and a dissipation phase. We calculate for each cloud the maximum cloud cooling, maximum areaexpansion of the anvil, and the final dissipation of the cloud (Futyan and Genio, 2007). Moreover, the 3D data allow us to derive the maximum vertical growth (Figure 2). We detect an average cooling (in terms of a change in reflectivity as depicted in Table 3)of 10–14 dBZ~~ (as outlined in Section 3.5), we check the point of time when three key events occur in each cloud trajectory: the maximum radar reflectivity gradient at 10 km ~~height (Figure 13,a). This cooling is enhanced for isolated clouds, particularly over the ocean, and over land for clustered clouds with $\geq$ 4 DCCs. We derive the~~ altitude ("reflectivity gradient"), the maximum cloud area growth ("area growth~~of the cloud anvil after the time of~~ "), and the ~~maximum cooling~~maximum vertical growth ("vertical growth"). Figure 13 shows the distribution of these indicators grouped by the surface type and number of cores. The average ~~growth for all clouds accounts for 20–60 % compared to the anvil area at CI. We find the highest values~~ maximum reflectivity gradient ranges from 10 to 16 dBZ. Clouds with 2–3 cores show the highest gradients (14.5–16 dBZ), while the gradient for single-core clouds averages around 14 dBZ. It decreases with further increasing core count, dropping to around 10 dBZ for clouds with ~~more than 5 DCCs. The vertical growth shows a reversed pattern as clouds with fewer DCCs tend to have astronger vertical growth between CI and the time of maximum cooling~~ 10 or more cores. Surface type has little impact overall, though values are slightly higher over the ocean for clouds with 1–3 cores (Figure 13, a). In contrast, cloud area growth is slightly higher over land. More important, clouds

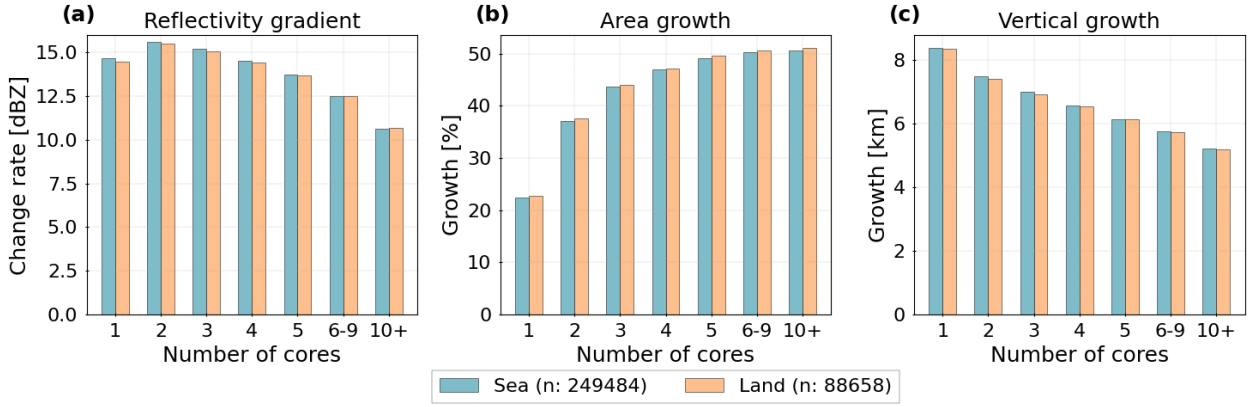

Figure 13. Life-cycle ~~phase transition~~ statistics grouped by the surface type and the number of associated cores for **(a)** the ~~maximum cooling~~ radar reflectivity gradient at 10 km height, **(b)** the relative area ~~expansion~~growth, and **(c)** the vertical growth of the cloud.

with multiple cores grow considerably more in area than single-core clouds - ranging from 22 % (single-core) to 52 % (10 and more cores) (Figure 13, ~~c~~b). For ~~all clouds, the growth of the anvil and~~ the vertical growth~~are higher over land due to a more pronounced thermal instability and surface heating during the day(Takahashi et al., 2017)~~, we observe average values between 5–8 km. Single-core clouds tend to grow higher than multi-core clouds, with only minor differences between land and sea (Figure 13, c).

~~In Fig. 14, we compare the convective cloud~~ We use Spearman's rank correlation coefficent R to examine relationships between life-cycle ~~grouped by~~ metrics and cloud/core properties for all cloud tracks, single-core, and multi-core clouds. Overall, cloud and core properties show predominantly positive correlations. The strongest correlation across all datasets appears between CTH and core height. Additional strong correlations include the number of ~~DCCs. For that purpose, we derive the time of transition between the three life-cycle phases and~~ cores with the cloud area and the core height. In contrast, cloud lifetime shows weak to moderate correlations (Figure 14, a). For single-core clouds, the ~~dissipation time for each group. Additionally, we include the life-cycle of the cloud clustering by assessing the time when we find the most and largest DCCs. Overall, we observe a broadening distribution and a shift towards a later occurrence for each phase with increasing numbers of DCCs. Multiple peaks characterise the distribution~~ correlation between cloud area and core height weakens, while the link between core area and cloud area strengthens (Figure 14, b). Multi-core clouds exhibit similar patterns to all cloud tracks, though with slightly weaker correlations (Figure 14, c). The number of cores correlates positively with area growth but negatively with both reflectivity gradient and vertical growth. Reflectivity gradient shows a weak positive correlation with area growth (< 0.25) and a stronger one with vertical growth (up to 0.5 for multi-core clouds). Area growth and vertical growth are negatively correlated, with medium to strong correlations. The relationship between the reflectivity gradient and other cloud properties is weak, and its direction differs by cloud type — positive for single-core~~clouds. In contrast, clustered clouds show a smoother uni- to bimodal distribution. In all cases, the average time of maximum cooling and maximum vertical growth~~

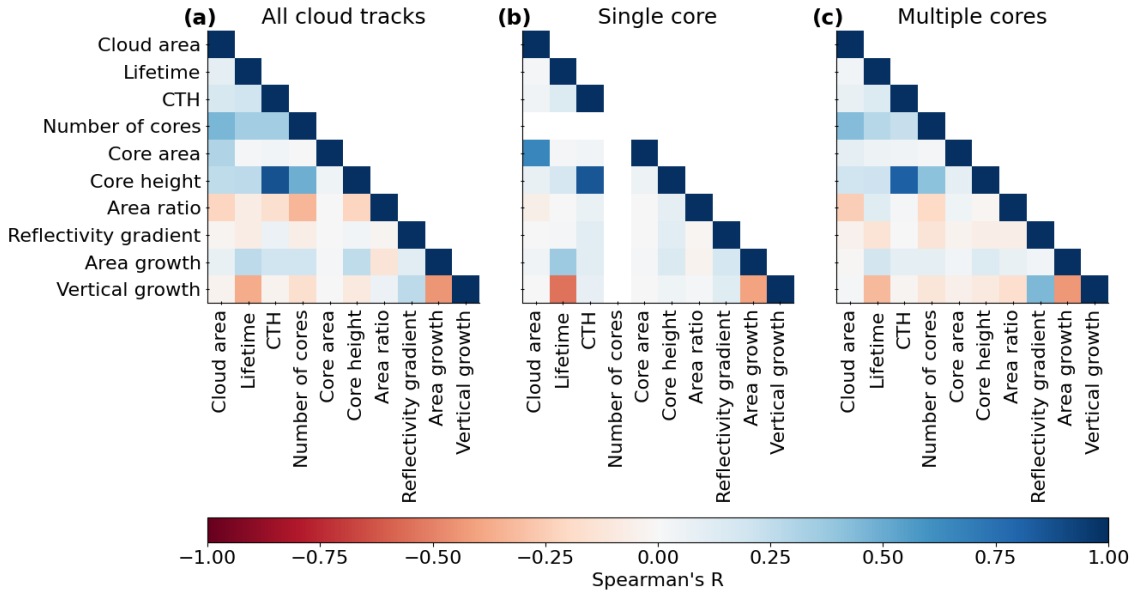

Figure 14. Correlation matrix for the life-cycle statistics, cloud and core properties. We calculate Spearman's R to quantify the correlation coefficient on a scale between -1 and 1 for **(a)** the whole dataset (n = 338,142), **(b)** clouds with a single core (n = 216,798), and **(c)** clouds with multiple cores (n = 121,344).

~~occurs before the maximum area growth. This finding indicates that the anvils continue growing beyond the time of maximum convective activity. All~~ , negative for multi-core clouds. Area growth correlates positively with cloud and core properties, especially the cloud lifetime. Vertical growth shows a negative correlation with cloud lifetime and mixed, generally weak correlations with cloud area, CTH, and core metrics.

Figure 15 presents the average timing (post-detection) of life-cycle statistics, grouped by surface type and core count. Here, we compute the average time after detection when the clouds reach their maximum ~~core size before the time of the maximum anvil area growth. In contrast to the core size, the time of the maximum core number varies with the number of DCCs. For less clustered clouds,~~ for the reflectivity gradient, anvil growth, vertical growth, number of cores, and core area. Moreover, we derive the time of ~~the maximum core number and the maximum vertical growth are similar. With a higher degree of organisation, the maximum number of cores appears after the maximum~~ dissipation which marks the end of the cloud life-cycle.

- Reflectivity gradient: Peaks around 0.85 h on average, with little difference for the median between land and sea. However, the distribution broadens over both surface types with increasing core numbers. The arithmetic mean increases up to 2.5–3 h for clouds with 10 and more cores (Figure 15, a).

- Area growth: Occurs at 1.64 h on average. Single-core clouds peak earlier (< 1.5 h), while multi-core clouds range from 1.7 h (2 cores) to 4 h (10 and more cores). For clouds with 3–5 cores, we find a predominantly similar distribution with only slight variations of the arithmetic mean (Figure 15, b).

- Vertical growth: Peaks around 1.19 h. This occurs earlier for single-core and oceanic clouds. For clouds with 4 (5) or more cores over land (sea), the distributions are similar and show only a weak variability (Figure 15, c).

- Core area & core number: The maximum core area typically occurs 1.25 h after detection, while the core number peaks slightly later at 1.37 h. Surface type has little effect on the time of the maximum core area, though the timing increases with more cores (Figure 15, d). Clouds over land - especially those with 2–5 cores - reach their maximum number of cores later than oceanic clouds. Despite this observation, we find less of a linear timing increase compared to other life-cycle statistics (Figure 15, e).

- Cloud dissipation: Clouds over land generally dissipate later than oceanic ones. Lifetime extends further with more cores, and value variability is also higher over land. Single-core clouds typically dissipate within 1–3 hours, whereas multi-core clouds last longer, with broader distributions and higher mean lifetimes (Figure 15, f).

Notably, the analysis shows that vertical growth may peak after the reflectivity gradient but before area growth. The ~~continuous interaction of convective cores within clustered cloudsmay prolong~~ times stretch for multi-core clouds, while single-core systems exhibit more compact timelines. However, outliers may distort observed mean values. Hence, the consecutive order of the life-cycle ~~due to a regeneration of convective intensity (Takahashi et al., 2017). As the cloud lifetime increases with the number of associated cores, the cooling~~ statistics may be affected by a high variability in the distribution. Across all cloud tracks, core number and core area tend to peak between vertical and area growth ~~appear earlier during the relative cloud lifetime. Clustered clouds spend more of their~~ maxima. However, the distributions show a high variability, especially for multi-core clouds and clouds over land. While we observe life-cycle ~~in a dissipating phase with a warming, shrinking anvil than a single-core cloud. As $\geq$ 80 % of detected clouds contain a single DCC, these isolated clouds considerably affect the mean calculated for all clouds (Section 4.1)~~statistics occurring on average later for clouds over land, the differences induced by the surface type remain overall low.

~~In Fig. 15, we analyse the diurnal cycle for the maximum cooling,~~

4.3.2 Temporal variability of life-cycle statistics

Figure 16 illustrates the diurnal patterns of the reflectivity gradient, the area growth, and ~~vertical growth grouped by the surface typefor isolated and clustered clouds. The distribution of these life-cycle statistics is similar to the diurnal convective cloud development over land and sea (Cui et al., 2021). We observe a morning peak followed by a decrease in the afternoon for the maximum cooling and vertical growth, particularly for~~ the vertical growth for single-core and multi-core clouds, grouped by surface type. Similar to results from Sect. 4.2.1, the diurnal cycle is more pronounced over land than over the ocean. The reflectivity gradient exhibits short-term fluctuations with noticeable nocturnal peaks around 20:00–21:00 UTC and 00:00–01:00 UTC, followed by decreases. During the day, peaks occur between 09:00–12:00 UTC and around 16:00 UTC, with a negative dip around noon (land) and 18:00 UTC (both land and sea). Over the ocean, the reflectivity gradient is generally higher and shows a slightly weaker variability than over land. Over land, multi-core clouds exhibit stronger gradients than single-core clouds. ~~A subsequent anvil area growth follows cooling phase (Figure 14)~~Distinct land-based negative peaks occur around

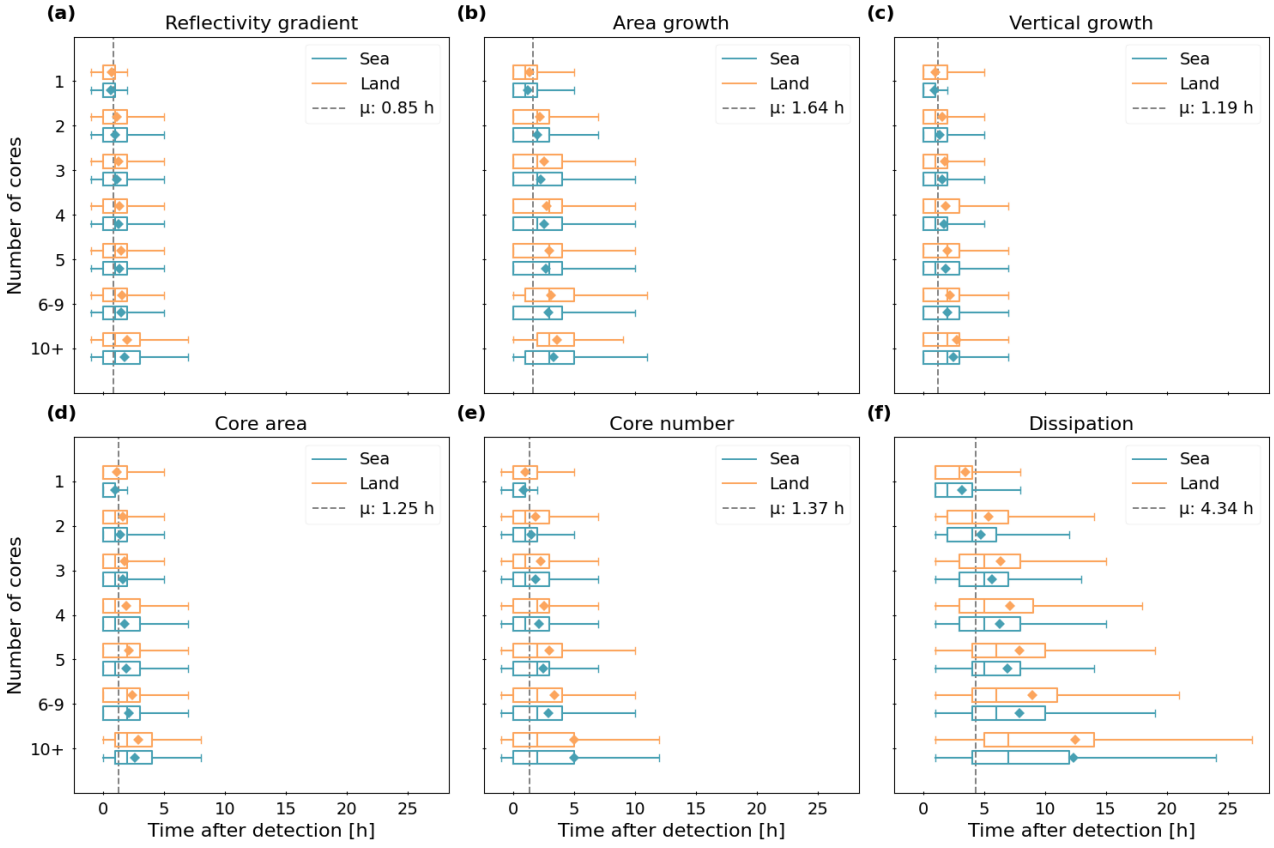

Figure 15. ~~Ridgeplot showing~~ Distribution of the time dependency (x-axis) ~~of~~ for the life-cycle ~~phase transition~~ statistics. The boxplot diagrams show the time after detection (in h) when the detected clouds reach on average the maximum value for **(a)** the ~~maximum cooling~~ radar reflectivity gradient at 10 km height, **(b)** the ~~maximum~~ vertical growth, **(c)** the ~~maximum~~ anvil growth, **(d)** the ~~maximum~~ core ~~size~~area, and **(e)** the ~~maximum~~ core number. Moreover, ~~and **(f)**~~ we show the average **(f)** dissipation time. Clouds are grouped by the surface type and number of cores (y-axis). The boxplot contains the median (bold blue or orange lines) and the arithmetic mean (blue or orange diamonds). The grey vertical lines show the mean time ~~for~~ dependency averaged over all clouds ~~, the red triangles the mean for each DCC group~~tracks.

03:00–06:00, 08:00, and 11:00–15:00 UTC. Over the ocean, we ~~observe a weak diurnal cycle with a primary peak in the late afternoon and a secondary peak at night. Overall , the vertical growth and absolute cooling are stronger for isolated clouds (Figure 15, a–c). Clouds with a single core show a reflectivity difference of up to 14 dBZ between CI and MAT and a vertical growth of 5.6–7 km. With an increasing number of DCCs, the total cooling and vertical growth of each DCC decreases as prior convective activity already induced a higher average radar reflectivity. In contrast, the anvil growth is on average 15 % higher for clustered systems. All continental clouds show a maximum anvil growth in the early afternoon.~~ find a weaker nocturnal peak at 01:00 UTC and a gradual increase between 06:00–20:00 UTC. Overall diurnal variability ranges from 0.5 dBZ (ocean) to 1 dBZ (land), or roughly 8–16 % of the mean gradient range (10–16 dBZ) (Figure 16, a, d). Multi-core clouds show significantly greater area growth (42–48 %) than single-core clouds (20–27 %). Over the ~~ocean,~~ ocean, we see sporadic daytime peaks that occur around 15:00, 20:00, and 01:00 UTC. Over land, area growth increases steadily for single-core clouds in the ~~diurnal peaks are weaker with a slight shift towards the late afternoon and early evening (Figure 15~~morning and peaks between 12:00–14:00 UTC. For multi-core clouds, we find several sporadic peaks during the day, similar to clouds over the ocean. Evening peaks appear around 18:00 and 22:00 UTC for multi-core clouds, and 20:00 UTC for single-core clouds. Diurnal variability remains low, ranging up to 5 % over both land and sea (Figure 16, b, e).

~~Diurnal cycle for the indicators showing the transition between cloud life-cycle phases. The data is grouped by the number of associated cores and the surface type. We display the hourly changes regarding **(a)** & **(d)** the maximum cooling, **(b)** & **(c)** the cloud anvil area growth, and **(c)** & **(f)** the cloud vertical growth for single- (1 DCC) and multi-core (>1 DCC) clouds over sea and land. Line plots show the mean value with a confidence interval of 95 %.~~

~~The seasonal cycle shows an increased cooling of about 2 dBZ and vertical growth of about~~ Diurnal variation in vertical growth is weak over the ocean with values below 0.5 km. Over land, morning peaks are evident, particularly for single-core clouds, while all cloud types show a distinct dip around noon. Afternoon and evening values rise again, with multiple peaks (e.g., 17:00, 21:00, 06:00 UTC) and troughs (18:00, 22:00, 03:00 UTC), typically within a 1–1.5 km ~~between spring and summer~~ variability range. Over both surface types, single-core clouds reach higher altitudes (7.5–8.75 km) than multi-core clouds (6.25–7.5 km) (Figure 16~~). For~~ , c, f).

Figure 17 presents monthly changes for the reflectivity gradient, the area growth, ~~we see an increase between 5–10 % for clustered~~ and the vertical growth between March and August 2019 for single- and multi-core clouds over land and sea~~and a decrease of 3–10 % for isolated cells over land . Throughout the time series, the cooling and vertical growth are higher for clouds with a single core. Clustered clouds have a weaker maximum cooling and vertical growth~~ . Overall, reflectivity gradients increase from March to August. For single-core clouds, the increase is more pronounced over the ocean (from 14.3 to 15.8 dBZ) than over land (13.5 to 14.25 dBZ). For multi-core clouds, values over land rise more (14.3 to 14.6 dBZ) than over the ocean (14.5 to 14.6 dBZ). A notable dip occurs across all cloud types in April. Month-to-month variability is high (Figure 17, a, d). Between March and June, area growth is higher over land, peaking in May for single-core and in June for multi-core clouds. ~~However, they show a more extensive area growth. A higher cooling, horizontal, and~~ After June, area growth becomes higher over the ocean. Over the period, single-core clouds over land show a net decline (around 3 %), while values increase slightly over the ocean (around 5 %) and for multi-core clouds over land (around 3 %). Monthly changes appear to be nonlinear and

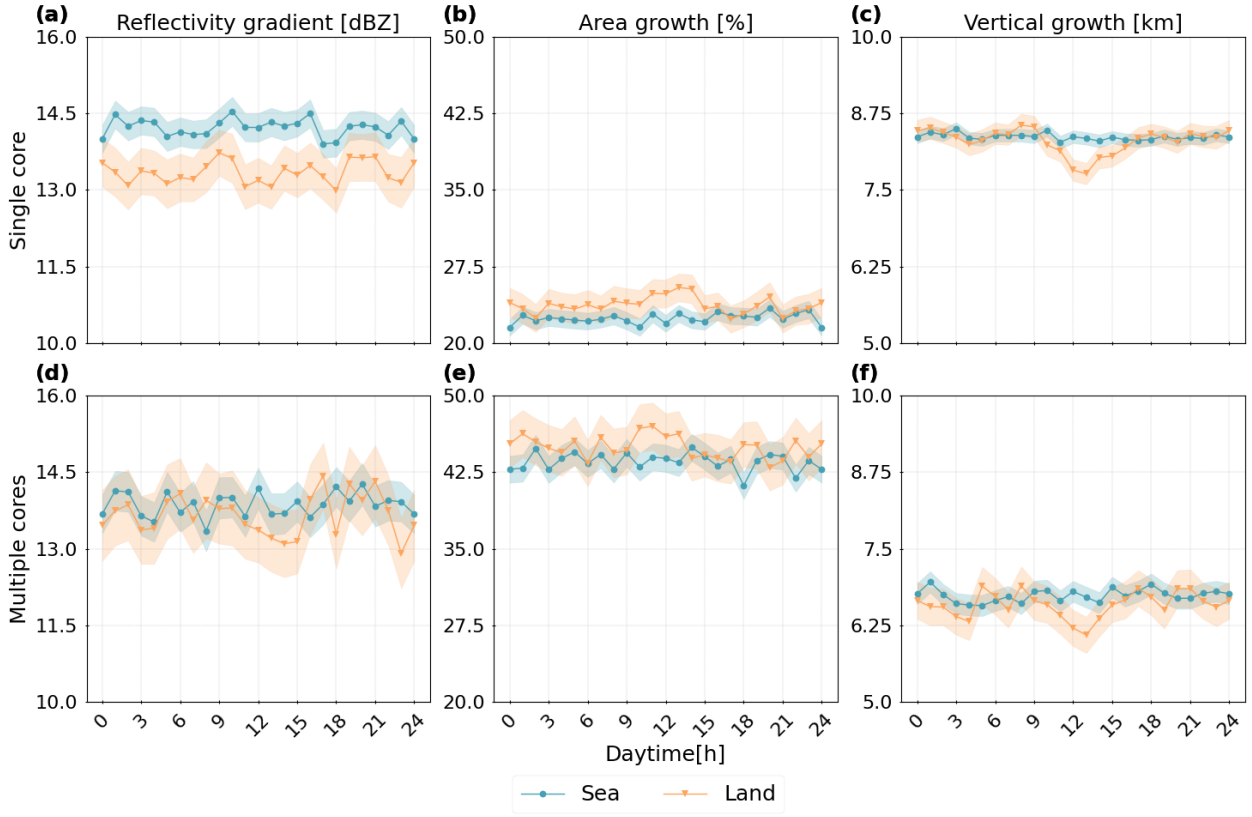

Figure 16. Diurnal cycle for the life-cycle statistics. We display the hourly changes (in UTC) regarding **(a)** & **(d)** the maximum cooling, **(b)** & **(e)** the cloud area growth, and **(c)** & **(f)** the cloud vertical growth for single- (1 core) and multi-core (>1 core) clouds over sea and land. Line plots show the mean value with a confidence interval of 95 %.

fluctuate considerably (Figure 17, b, e). The vertical growth of ~~clustered clouds is associated with higher convective activity and more intense DCCs. While convective activity increases~~ single-core clouds peaks in March, drops sharply in April. From May onward, it rises again over land and decreases over the ocean~~in summer, we still detect more intense changes in the~~ . The total change ranges between 0.5–1 km. Early in the period, oceanic clouds have a higher vertical growth than clouds over land. From June onward, this pattern reverses (Figure 17, c, f). Throughout the study period, single-core clouds consistently show higher reflectivity gradients and vertical growth, while multi-core clouds exhibit greater area growth. Though the surface type may influence these statistics, the observed effect in our study remains relatively small. In contrast, the number of cores plays a more substantial role in shaping the cloud ~~life-cycle over land(Figure 15, 16). The difference may be due to a higher variability of the moisture availability over land and an enhanced orographic forcing (Chen et al., 2021)~~life-cycle.

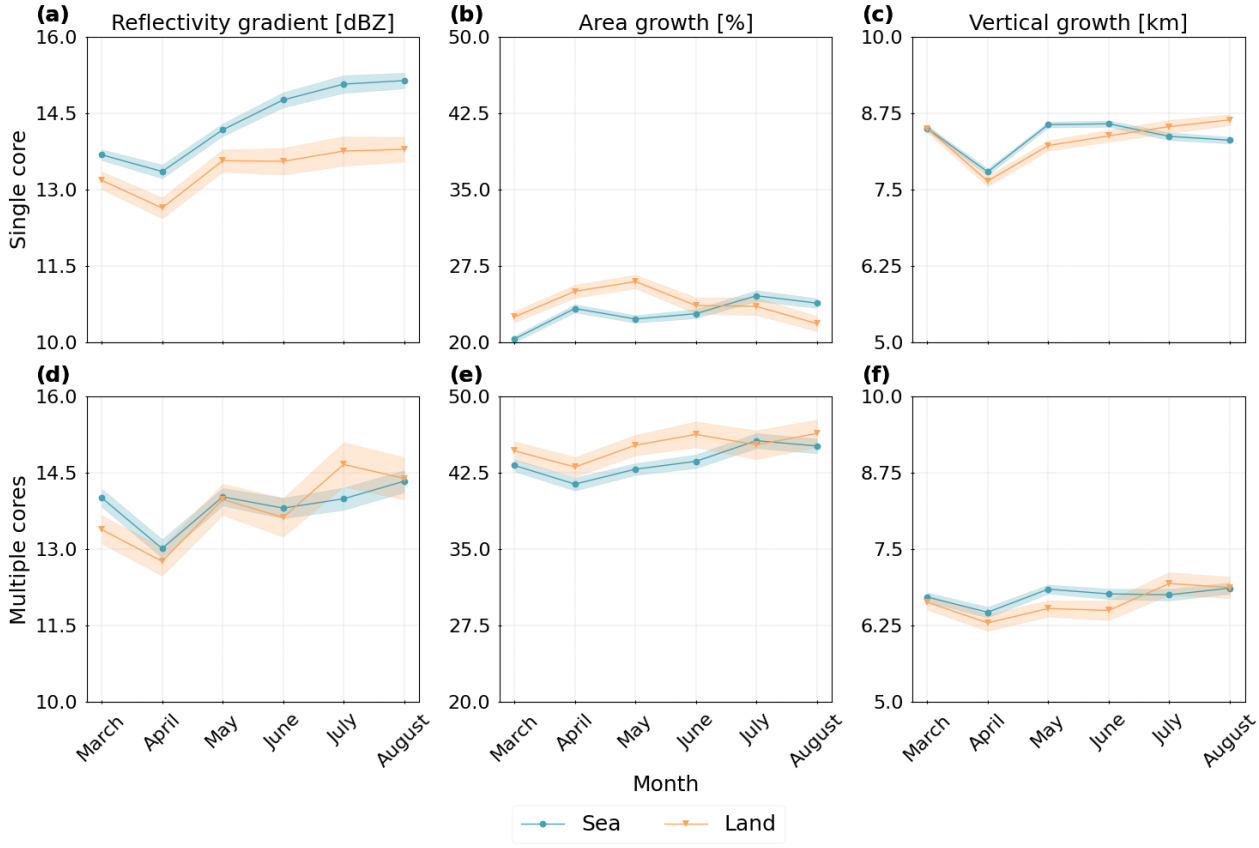

Figure 17. ~~Seasonal cycle~~ Monthly changes for the ~~indicators showing the transition between cloud~~ life-cycle ~~phases. The data is grouped by the number of associated cores and the surface type~~statistics. In **(a)** & **(d)**, we show the maximum cooling, in **(b)** & **(e)** the anvil area growth, and in **(c)** & **(f)** the vertical growth for clouds with a single (1 ~~DCC~~core) core or multiple (>1 ~~DCC~~core) cores. Line plots show the mean value with a confidence interval of 95 %.

5 Discussion

~~Our analysis provides a detailed perspective on the temporal variability of deep convective cells and associated core regions derived from ML-based~~

5.1 Summary of results

In this study, we use a ML–based 3D ~~radar reflectivities. In previous studies, retrievals of DCCs often originate~~ extrapolation of radar reflectivity, derived from 2D ~~data, either from geostationary satellites (Jones et al., 2024; Vondou, 2012) or from active radar, such as the CloudSat CPR (Igel et al., 2014; Takahashi et al., 2017). These approaches are limited to comprise either a specific horizontal or vertical dimension. As a result, they cannot provide a seamless coverage of the cloud development.~~

~~With geostationary satellites, we can approximate the cloud vertical depth using the WV channels. However, the results may insufficiently differentiate between cirrus and convective clouds (Masunaga and Luo, 2016). Our study allows us to cover the cloud development along three dimensions. Compared to the results by Takahashi et al. (2023) , we detect a substantially~~ satellite imagery, to characterise single- and multi-core convective clouds in the tropics. Our analysis shows that the majority of detected clouds are short-lived (under three hours) and dominated by a single core (65 %). Compared to multi-core clouds, these single-core systems tend to have a smaller cloud area, lower reflectivity at 10 km, and reduced CTH. Their cores are also typically smaller, shorter-lived, and lower in altitude — though they exhibit a higher area ratio between cloud and core area. In contrast, multi-core systems a larger in area, persist longer, reach a greater CTH and core height, and form larger individual cores (Section 4.1). Correlation analysis reveals a high interdependence among cloud and core properties. The strongest positive relationships are found between CTH and core height, and between the number of cores and both cloud area and core height (Figure 14).

Over land, the diurnal cycle exhibits a midday-to-afternoon peak (12:00–16:00 UTC) for the cloud and core area, the reflectivity at 10 km, the core height, and area ratio, with a secondary overnight peak for the cloud and core lifetimes. Over the ocean, the diurnal cycle is less pronounced but still shows afternoon, evening, and nighttime maxima. These patterns are especially distinct for single-core clouds (Section 4.2) and are largely consistent with prior tropical observations (e.g., Chen et al. (2021); Takahashi et al. (2017); Gupta et al. (2024)). Derived life-cycle statistics indicate that peaks for the reflectivity gradient typically precede vertical growth and subsequent area expansion — mainly around local noon and early evening over continental Africa. In oceanic regions, a less consistent pattern emerges, with a high variability throughout the day (Section 4.3.2). Compared to Wilcox et al. (2023), we observe weaker diurnal amplitudes over both land and ocean; however, the differences between single- and multi-core clouds are more pronounced than those between land- and sea-based convection.

We also find that changes in cloud area, core number, and cloud height often evolve in line with an idealised convective life cycle described in Sect. 3.5. Longer-lived clouds tend to exhibit more cores and larger maximum core areas. Multi-core systems reach their peak core number and core size later in their life cycle than single-core clouds (Section 4.3.1). The reflectivity gradients correlate positively with vertical growth and negatively with area expansion, reflecting transitions from development to maturity, as noted by Hu et al. (2021). Single-core clouds display stronger vertical ascent and higher reflectivity gradients, though most correlations are weak — aside from a strong negative relationship between cloud lifetime and vertical growth, and a moderate positive link between lifetime and area growth. For multi-core systems, average area growth is about 20–30 % higher than for single-core clouds. Reflectivity gradient and vertical growth are negatively correlated with most other properties, while the area growth shows positive correlations with the core count, core area, and core height. However, correlations differ between single-core and multi-core systems (Figure 13, Figure 14). Finally, our results underscore how differences in core structure and number may influence convective cloud development and the associated life-cycle.

5.2 Influences on convective clouds in the tropics

Compared to previous studies by Takahashi et al. (2023) and Hu et al. (2021), our analysis identifies a significantly higher number of ~~cloud tracks with at least one DCC. With the ML model, we have the potential to achieve global predictions of~~

the radar reflectivity and reduce the false detection of convective cellspotentially convective cloud tracks. The derived cloud characteristics align well with aircraft observations (Zipser and LeMone, 1980) and precipitation-based studies (Zipser et al., 2006) . Over tropical Africa, our core distribution results are consistent with those derived for geostationary satellite data (Jones et al., 2024) or the CloudSat CPR Deng et al. (2016), both of which found a high prevalence of clouds with one to three cores. Similarly, Pilewskie and L'Ecuyer (2022) reported that one-third to half of convective systems observed globally by the CloudSat CPR contain a single core. For the tropics, however, our results are in closer agreement. In line with these findings, we observe that cloud area generally increases with the number of cores. However, this relationship exhibits substantial variability, especially in multi-core systems (Section 4.3.1).

5.3 Regional influences on the cloud life-cycle

Our results are consistent with measurements from cloud-penetrating aircraft (LeMone and Zipser, 1980) or the analysis of precipitation data (Zipser et al., 2006). Clustered clouds regenerate their convective activity in response Our results show that convective cloud properties over land typically peak during the day, while over the ocean, we observe two peaks during daytime and at night (Sect. 4.2.1). These findings align with the diurnal cycle of tropical convection (Vondou, 2012; Takahashi et al., 2023) . A nocturnal enhancement over the ocean may be linked to the diurnal forcing of surface heating (Futyan and Genio, 2007). Most MCSs initiate during daytime, which points toward the importance of local surface characteristics for the propagation of convective organisation (Vondou, 2012; Takahashi et al., 2023). With the onset of the WAM, convective systems may sustain through the night as the nocturnal surface cooling is reduced for clustered clouds (Futyan and Genio, 2007). The diurnal cycle of cycle of free-tropospheric relative humidity maximises at night over the tropical oceans and alters convective activity. While a higher relative humidity reduces the entrainment into convective plumes, it allows convective air parcels to maintain their buoyancy longer as they rise, producing deeper convective towers (Wall et al., 2020). For instance, our results suggest a connection between the seasonal cycle of convection and the surface type. Convective storms develop during the rainy season in the mountainous highlands and move into the basin at night when katabatic flow prevails (Nicholson, 2018). Within the AOI, convective activity frequently occurs. Developing clouds may travel large distances due to a contiguous advection towards the Atlantic Ocean. humidity, which peaks overnight and supports convection (Wall et al., 2020). After sunrise, solar heating may stabilize the atmosphere. A weakening land breeze may lead to the dissipation of night-time clusters (Houze Jr., 2004). While these diurnal patterns may be reflected by the cloud properties (Sections 4.2.1), differences in the daytime of the first detection for the cloud tracks appear weaker (Figure 9). Throughout the day, we observe several peaks for the reflectivity gradient, followed by phases of vertical and horizontal cloud growth (Section 4.3.2). Notably, as the number of cores increases, both reflectivity gradient and vertical growth decline, while area growth becomes more pronounced (Section 4.3.1). This finding may correspond to a higher reflectivity at 10 km and broader spatial extent seen for multi-core systems (Section 4.1). Our observations may point to a self-sustaining mechanism where cores are regenerated in response to diurnal heating (e.g., Deng et al. (2016); Hartmann et al. (2018); Takahashi et al. (2017)). However, quantifying the impact of local topography requires further research. Thermal contrasts and diurnal circulation patterns drive the land-ocean differences (Li et al., 2021). We

emphasise that the interaction between DCCs affects the life-cycle of clustered convection substantially. A prolonged lifetime may induce a repeated vertical updraft we did not explicitly investigate this process.

Seasonal variability in tropical convection has been highlighted in past studies. For example, multi-core systems often persist overnight during the onset of the West African Monsoon (Futyan and Genio, 2007). During this period, convection may frequently initiate over high terrain and propagate downslope at night under katabatic flow (Nicholson, 2018). While our results may be influenced by interannual variability, as the dataset spans only one year and does not capture a full annual cycle, we may observe temporal changes in cloud and core properties between March and August. For instance, we find an increase of the cloud area, cloud lifetime, number of cores, and core area over the ocean. Over land, these properties slightly decrease (Section 4.2.2). Reflectivity gradients increase along the period, in particular over the ocean, while vertical and area growth . Following the results by Takahashi et al. (2017) and Taylor et al. (2022)vary more considerably (Section 4.3.2). Between June and August, we detect overall less clouds but proportionally more clouds over the ocean. However, differences between monthly averages over both surface types remain small. Here, our results may diverge from studies that report more pronounced spatial and seasonal variations for convective clouds over land and sea (e.g., Takahashi and Luo (2012); Wilcox et al. (2023)). More striking than these surface-type induced differences in mean cloud properties are the contrasts between single- and multi-core clouds. Longer-lived, multi-core systems often exhibit repeated phases of growth (Takahashi et al., 2017). Consistent with Taylor et al. (2017), we observe more intense DCCs and increased growth of the cloud core and anvil slightly larger cores, especially between March and May, and enhanced area growth for continental convection (Section 4.2.2). At the edges of the AOI, extratropical effects may come into play and affect the cloud life-cycle (Jones et al., 2024). Disentangling the impact of convective processes within the tropics and mid-latitudes remains a challenge and requires an extensive AOI. Sections 4.2.2 and 4.3.2).

5.3 Limitations and future challenges

Our analysis is based on ML-derived 3D radar reflectivity fields. While the results may help to extend the data availability of global radar reflectivities, they possibly contribute to mitigating limitations in approximating the cloud vertical extent from geostationary satellite observations. However, we point out several important limitations. The input data for the ML model originate from the are based on observations from the Cloud Profiling Radar (CPR) aboard the CloudSat satellite, which lacks sensitivity to observe has known limitations in detecting ice clouds due to an underestimation of the topmost outflow height (Wang et al., 2014). Our results show this limitation in terms of a weak representation of shallow convectionand cirrus clouds. Recently released instruments like the flexible combined imager (Holmlund et al., 2021) aboard its tendency to underestimate the height of upper-level outflow (Wang et al., 2014). Additionally, signal attenuation near the surface caused by topography reduces the CPR's sensitivity to shallow convection. As a result, our analysis underrepresents both shallow convective and cirrus cloud types. Emerging satellite systems, such as the Flexible Combined Imager on the Meteosat Third Generation (MTG) satellite system or the spatio-temporal enhanced CPR of the Earth Cloud Aerosol and Radiation Explorer (EarthCARE) mission (Eisinger et al., 2024)have a higher platform (Holmlund et al., 2021) and the enhanced CPR on the EarthCARE mission (Eisinger et al., 2024), offer improved spatial and temporal resolution. The data may allow for a more

accurate detection of clustered MCSs and small-scale changes during their These instruments are expected to enhance the detection and characterisation of the convective cloud life-cycle. In the current study, we did not examine some presumably important influences like the effect of aerosols, the Moroever, our study does not account for several potentially important influences on convection, such as aerosol interactions, vertical wind shear, or the entrainment rate (Masunaga and Luo, 2016). Including these factors may help to further understand the drivers of convective organisation. We chose the *tobac* framework to detect and entrainment rates (Masunaga and Luo, 2016). Incorporating these factors in future analyses could lead to a more comprehensive understanding of convective processes. Our study focuses on a domain within the tropical band from 30° W to 30° E and 30° N to 30° S. As extratropical influences may blur the statistics at the domain's northern and southern edges, it may be beneficial to explore the intra-tropical variability and the role of large-scale dynamics beyond this region to distinguish tropical from midlatitude convective processes.

To identify isolated and clustered convective clouds (Sokolowsky et al., 2024). Nevertheless, we note that no universal systems, we employ the *tobac* framework (Sokolowsky et al., 2024). However, this object-based approach relies on manually set thresholds for the detection, introducing a degree of subjectivity that may influence the resulting cloud statistics. This includes potential limitations in the analysis of the cloud life-cycle, which itself does not provide insights on actual changes of the cloud temperature. It is important to emphasise that no universally optimal detection algorithm exists (Lakshmanan and Kain, 2010). Instead, every algorithm has specific benefits ; each method has context-specific strengths and limitations depending on the use case and study area (Prein et al., 2024). Despite our ability to achieve intended application and geographic domain (Prein et al., 2024). While our approach may enable an approximation of the vertical updraft by the radar reflectivity , it cannot replace a calculation cloud column, radar reflectivity alone does not substitute for measurements of vertical wind shear (Luo et al., 2008). Although the effect of vertical shear within the tropics is expected to be minor compared to the mid-latitudes, its quantification requires further analysis (Takahashi et al., 2017). Moreover, investigating precipitation patterns associated with clustered convection could lead to a more accurate forecast of extreme events (Kukulies et al., 2021). However, further research is required to sufficiently assess the present and future risks associated with MCSs vertical shear may have a smaller impact on convective processes in the tropics than in mid-latitude regions, its role still warrants further investigation (Takahashi et al., 2017). Finally, to better assess current and future convective risks, particularly those posed by multi-core systems, future work should explore their associated precipitation patterns in more depth (Atiah et al., 2023).

6 Conclusions

This study analysed the analyses the properties and life-cycle of convective clouds and their deep convective cores over a tropical region covering the Atlantic Ocean and West Africa. Using an ML-based extrapolation of radar reflectivities, we could detect and may enhance the number of detected clouds compared to retrievals from CloudSat CPR alone. Hence, the approach may help to close current data gaps. In this study, we aim to showcase the 3D data and their ability to track convective clouds in 3D throughout all stages of the cloud and cores along their life-cycle. Compared to using data from a single only either a passive or active sensor, our perspective allows may allow a simultaneous coverage of cloud development in the horizontal and

vertical ~~dimensions. Tropical convection appears more intense over land than over the ocean. Over continental Africa, we find more long-lasting clouds with multiple deep convective cores. Within these clouds, core interactions impact the intensity and lifetime of~~ dimension.

The results suggest that differences based on the number of cores are higher than the ~~cloud cluster and its life-cycle. Overall, we detect substantial seasonal differences for clouds over both surface types. Convective activity increases in summer, particularly for clustered clouds over the ocean. However, changes~~ surface-type induced variability. Single-core clouds develop and dissipate on shorter timescales. They have a smaller cloud and core area, and lower CTH and core height than multi-core systems. The longer cloud lifetime of multi-core clouds may be associated to a later occurrence of the maximum number of cores and core area. Between single-core and multi-core clouds, we find considerable differences in the cloud ~~life-cycle, like the anvil area growth, remain stronger over land during the whole period. With a higher degree of organisation, the interaction of adjacent cores may drive a renewal of convective activity. This leads to a a prolonged cloud~~ life-cycle ~~and a later occurring~~ statistics regarding the changes in the radar reflectivity at 10 km height, the vertical growth, and the area growth of the cloud. While the former two are higher for clouds with a single core, multi-core cloud clusters with a larger cloud area tend to grow more along the horizontal dimension. The more cores we find, the later the maximum number of ~~DCCs. Isolated convective cells have a higher cooling and more extensive vertical growth than clustered clouds. Nonetheless, they persist predominately for a short time and show weaker convective activity than clustered systems.~~ cores and the maximum core area occur. While the differences between the convective clouds over land and ocean are lower than expected, we emphasise our analysis uses six months of data and may not represent the annual cycle of convection. Nevertheless, expanding the approach to investigate a longer time series may account for current uncertainties.

In this work, we use the number of convective cores ~~as a single proxy for convective organisation~~to compare the effects of spatial clustering. However, ~~it may be~~ we think that it is worth comparing these results to a quantification of convective organisation using more advanced metrics, as done in the accompanying manuscript~~. The analysis shows a high variability and ambiguous results over different surface types, in particular during the summer season. Expanding the analysis by an investigation of spatial patterns of convective organisation may account for current uncertainties induced by a surface type specific seasonality~~.

Code and data availability. The level 2B-GEOPROF CloudSat data used in this study are available at the CloudSat Data Processing Center at CIRA/Colorado State University and can be retrieved from http://www.CloudSat.cira.colostate.edu/order-data (CloudSat Data Processing Center, 2024). The Meteosat SEVIRI level 1.5 data used in this study is freely and openly available via the EUMETSAT Data Store at https://navigator.eumetsat.int/product/EO-:EUM:DAT:MSG:HRSEVIRI (EUMETSAT Data Services, 2024). The code used in this study will be released upon publication.

Author contributions. S.B and H.T. designed the study. S.B developed the code for the analysis and visualisation. S.B. and H.T. contributed to the analysis and evaluation of cloud tracks and properties. S.B. and H.T. wrote the draft of the paper. All authors have read and agreed to the published version of the manuscript.

Competing interests. The authors declare that they have no conflict of interest.

Acknowledgements. This work was supported by the project "Big Data in Atmospheric Physics (BINARY)", funded by the Carl Zeiss Foundation (grant P2018-02-003), and the Max Planck Graduate Center with the Johannes Gutenberg University of Mainz (MPGC). We thank EUMETSAT for providing access to the Meteosat SEVIRI imager data and the Cooperative Institute for Research in the Atmosphere, CSU, for providing access to the CloudSat 2B-GEOPROF data.

References

Andrews, P. C., Cook, K. H., and Vizy, E. K.: Mesoscale convective systems in the Congo Basin: seasonality, regionality, and diurnal cycles, Clim. Dyn., 62, 609–630, https://doi.org/10.1007/s00382-023-06903-7, 2024.

Atiah, W. A., Amekudzi, L. K., and Danuor, S. K.: Mesoscale convective systems and contributions to flood cases in Southern West Africa (SWA): A systematic review, Weather and Climate Extremes, 39, 100 551, https://doi.org/10.1016/j.wace.2023.100551, 2023.

Bacmeister, J. T. and Stephens, G. L.: Spatial statistics of likely convective clouds in CloudSat data, J. Geophys. Res. Atmos., 116, D04 104, https://doi.org/10.1029/2010JD014444, 2011.

Bony, S., Stevens, B., Frierson, D., Jakob, C., Kageyama, M., Pincus, R., Shepherd, T., Sherwood, S., Siebesma, A., Watanabe, M., and Webb, M.: Clouds, circulation and climate sensitivity, Nature Geoscience, 8, 261–268, https://doi.org/10.1038/ngeo2398, 2015.

Brüning, S., Niebler, S., and Tost, H.: Artificial intelligence (AI)-derived 3D cloud tomography from geostationary 2D satellite data, Atmos. Meas. Tech., 17, 961–978, https://doi.org/10.5194/amt-17-961-2024, 2024.

Chen, P.-J., Chen, W.-T., Wu, C.-M., and Yo, T.-S.: Convective Cloud Regimes From a Classification of Object-Based CloudSat Observations Over Asian-Australian Monsoon Areas, Geophys. Res. Lett., 48, e2021GL092 733, https://doi.org/10.1029/2021GL092733, 2021.

Chen, S. S. and Houze, R. A.: Diurnal variation and life-cycle of deep convective systems over the tropical pacific warm pool, Q. J. R. Meteorol. Soc., 123, 357–388, https://doi.org/10.1002/qj.49712353806, 1997.

CloudSat Data Processing Center: Data Products, CloudSat DPC [data set], https://www.cloudsat.cira.colostate.edu/data-products, accessed: 2024-12-12, 2024.

Cohen, J.: Statistical Power Analysis for the Behavioral Sciences, Routledge, 2 edn., https://doi.org/10.4324/9780203771587, 2013.

Crook, J., Klein, C., Folwell, S., Taylor, C. M., Parker, D. J., Stratton, R., and Stein, T.: Assessment of the Representation of West African Storm Lifecycles in Convection-Permitting Simulations, ESS, 6, 818–835, https://doi.org/10.1029/2018EA000491, 2019.

Cui, W., Dong, X., Xi, B., and Feng, Z.: Climatology of Linear Mesoscale Convective System Morphology in the United States Based on the Random-Forests Method, J. Clim., 34, 7257–7276, https://doi.org/10.1175/JCLI-D-20-0862.1, 2021.

Deng, M., Mace, G. G., and Wang, Z.: Anvil Productivities of Tropical Deep Convective Clusters and Their Regional Differences, Journal of the Atmospheric Sciences, 73, 3467 – 3487, https://doi.org/10.1175/JAS-D-15-0239.1, 2016.

Dixon, M. and Wiener, G.: TITAN: Thunderstorm Identification, Tracking, Analysis, and Nowcasting—A Radar-based Methodology, J. Atmos. Oceanic Tech., 10, 785–797, https://doi.org/10.1175/1520-0426(1993)010<0785:TTITAA>2.0.CO;2, 1993.

Eisinger, M., Marnas, F., Wallace, K., Kubota, T., Tomiyama, N., Ohno, Y., Tanaka, T., Tomita, E., Wehr, T., and Bernaerts, D.: The Earth-CARE mission: science data processing chain overview, Atmos. Meas. Tech., 17, 839–862, https://doi.org/10.5194/amt-17-839-2024, 2024.

Esmaili, R. B., Tian, Y., Vila, D. A., and Kim, K.-M.: A Lagrangian analysis of cold cloud clusters and their life cycles with satellite observations, J. Geophys. Res. Atmos., 121, 11,723–11,738, https://doi.org/10.1002/2016JD025653, 2016.

EUMETSAT Data Services: High Rate SEVIRI Level 1.5 Image Data - MSG - 0 degree, https://navigator.eumetsat.int/product/EO:EUM:DAT:MSG:HRSEVIRI, accessed: 2024-12-12, 2024.

Feng, Z., Hardin, J., Barnes, H. C., Li, J., Leung, L. R., Varble, A., and Zhang, Z.: PyFLEXTRKR: a flexible feature tracking Python software for convective cloud analysis, Geosci. Model Dev., 16, 2753–2776, https://doi.org/10.5194/gmd-16-2753-2023, 2023.

Finkensieper, S., Meirink, J. F., van Zadelhoff, G.-J., Hanschmann, T., Benas, N., Stengel, M., Fuchs, P., Hollmann, R., Kaiser, J., and Werscheck, M.: CLAAS-2.1: CM SAF CLoud property dAtAset using SEVIRI - Edition 2.1, https://doi.org/10.5676/EUM_SAF_CM/CLAAS/V002_01, 2020.

Fiolleau, T. and Roca, R.: An Algorithm for the Detection and Tracking of Tropical Mesoscale Convective Systems Using Infrared Images From Geostationary Satellite, IEEE Trans. Geosci. Remote. Sens., 51, 4302–4315, https://doi.org/10.1109/TGRS.2012.2227762, 2013.

Futyan, J. M. and Genio, A. D. D.: Deep Convective System Evolution over Africa and the Tropical Atlantic, J. Clim., 20, 5041–5060, https://doi.org/10.1175/JCLI4297.1, 2007.

Gallus, W. A., Snook, N. A., and Johnson, E. V.: Spring and Summer Severe Weather Reports over the Midwest as a Function of Convective Mode: A Preliminary Study, WAF, 23, 101–113, https://doi.org/10.1175/2007WAF2006120.1, 2008.

Ganetis, S. A., Colle, B. A., Yuter, S. E., and Hoban, N. P.: Environmental Conditions Associated with Observed Snowband Structures within Northeast U.S. Winter Storms, Mon. Weather Rev., 146, 3675–3690, https://doi.org/10.1175/MWR-D-18-0054.1, 2018.

Guillaume, A., Kahn, B. H., Yue, Q., Fetzer, E. J., Wong, S., Manipon, G. J., Hua, H., and Wilson, B. D.: Horizontal and Vertical Scaling of Cloud Geometry Inferred from CloudSat Data, Journal of Atmospheric Sciences, 75, 2187–2197, https://doi.org/10.1175/JAS-D-17-0111.1, 2018.

Gupta, S., Wang, D., Giangrande, S. E., Biscaro, T. S., and Jensen, M. P.: Lifecycle of updrafts and mass flux in isolated deep convection over the Amazon rainforest: insights from cell tracking, Atmos. Chem. Phys., 24, 4487–4510, https://doi.org/10.5194/acp-24-4487-2024, 2024.

Haberlie, A. M. and Ashley, W. S.: A Method for Identifying Midlatitude Mesoscale Convective Systems in Radar Mosaics. Part II: Tracking, JAMC, 57, 1599–1621, https://doi.org/10.1175/JAMC-D-17-0294.1, 2018.

Hartmann, D. L., Hendon, H. H., and Houze, R. A.: Some Implications of the Mesoscale Circulations in Tropical Cloud Clusters for Large-Scale Dynamics and Climate, Journal of Atmospheric Sciences, 41, 113 – 121, https://doi.org/10.1175/1520-0469(1984)041<0113:SIOTMC>2.0.CO;2, 1984.

Hartmann, D. L., Gasparini, B., Berry, S. E., and Blossey, P. N.: The Life Cycle and Net Radiative Effect of Tropical Anvil Clouds, Journal of Advances in Modeling Earth Systems, 10, 3012–3029, https://doi.org/https://doi.org/10.1029/2018MS001484, 2018.

Haynes, J. M., L'Ecuyer, T. S., Stephens, G. L., Miller, S. D., Mitrescu, C., Wood, N. B., and Tanelli, S.: Rainfall retrieval over the ocean with spaceborne W-band radar, J. Geophys. Res. Atmos., 114, https://doi.org/10.1029/2008JD009973, 2009.

Heikenfeld, M., Marinescu, P. J., Christensen, M., Watson-Parris, D., Senf, F., van den Heever, S. C., and Stier, P.: tobac 1.2: towards a flexible framework for tracking and analysis of clouds in diverse datasets, Geosci. Model Dev., 12, 4551–4570, https://doi.org/10.5194/gmd-12-4551-2019, 2019.

Holmlund, K., Grandell, J., Schmetz, J., Stuhlmann, R., Bojkov, B., Munro, R., Lekouara, M., Coppens, D., Viticchie, B., August, T., Theodore, B., Watts, P., Dobber, M., Fowler, G., Bojinski, S., Schmid, A., Salonen, K., Tjemkes, S., Aminou, D., and Blythe, P.: Meteosat Third Generation (MTG): Continuation and Innovation of Observations from Geostationary Orbit, BAMS, 102, E990–E1015, https://doi.org/10.1175/BAMS-D-19-0304.1, 2021.

Horner, G. and Gryspeerdt, E.: The evolution of deep convective systems and their associated cirrus outflows, Atmos. Chem. Phys., 23, 14 239–14 253, https://doi.org/10.5194/acp-23-14239-2023, 2023.

Houze, R. A. and Hobbs, P. V.: Organization and Structure of Precipitating Cloud Systems, Adv. Geophys., 24, 225–315, https://doi.org/10.1016/S0065-2687(08)60521-X, 1982.

Houze Jr., R. A.: Observed structure of mesoscale convective systems and implications for large-scale heating, Q.J.R. Meteorol. Soc., 115, 425–461, https://doi.org/https://doi.org/10.1002/qj.49711548702, 1989.

Houze Jr., R. A.: Mesoscale convective systems, Rev. Geophys., 42, RG4003, https://doi.org/10.1029/2004RG000150, 2004.

Hu, X., Ge, J., Li, W., Du, J., Li, Q., and Mu, Q.: Vertical Structure of Tropical Deep Convective Systems at Different Life Stages From CloudSat Observations, Journal of Geophysical Research: Atmospheres, 126, e2021JD035 115, https://doi.org/https://doi.org/10.1029/2021JD035115, 2021.

Igel, M. R., Drager, A. J., and van den Heever, S. C.: A CloudSat Cloud-Object Partitioning Technique and Assessment and Integration of Deep Convective Anvil Sensitivities to Sea Surface Temperature, J. Geophys. Res. Atmos., 119, 10 515–10 535, https://doi.org/10.1002/2014JD021717, 2014.

Jackson, L. S., Marsham, J. H., Parker, D. J., Finney, D. L., Fitzpatrick, R. G. J., Rowell, D. P., Stratton, R. A., and Tucker, S.: The Effect of Explicit Convection on Climate Change in the West African Monsoon and Central West African Sahel Rainfall, J. Clim., 35, 1537–1557, https://doi.org/10.1175/JCLI-D-21-0258.1, 2022.

Jones, W., Christensen, M., and Stier, P.: A semi-Lagrangian method for detecting and tracking deep convective clouds in geostationary satellite observations, Atmos. Meas. Tech., 16, 1043–1059, https://doi.org/10.5194/amt-16-1043-2023, 2023.

Jones, W., Stengel, M., and Stier, P.: A Lagrangian perspective on the lifecycle and cloud radiative effect of deep convective clouds over Africa, Atmos. Chem. Phys., 24, 5165–5180, https://doi.org/10.5194/acp-24-5165-2024, 2024.

Kikuchi, M. and Suzuki, K.: Characterizing Vertical Particle Structure of Precipitating Cloud System From Multiplatform Measurements of A-Train Constellation, Geophysical Research Letters, 46, https://doi.org/10.1029/2018GL081244, 2019.

Kniffka, A., Knippertz, P., and Fink, A. H.: The role of low-level clouds in the West African monsoon system, Atmos. Chem. Phys., 19, 1623–1647, https://doi.org/10.5194/acp-19-1623-2019, 2019.

Kukulies, J., Chen, D., and Curio, J.: The Role of Mesoscale Convective Systems in Precipitation in the Tibetan Plateau Region, J. Geophys. Res. Atmos., 126, e2021JD035 279, https://doi.org/10.1029/2021JD035279, 2021.

Lakshmanan, V. and Kain, J. S.: A Gaussian Mixture Model Approach to Forecast Verification, WAF, 25, 908–920, https://doi.org/10.1175/2010WAF2222355.1, 2010.

Leary, C. A. and Houze, R. A.: The Contribution of Mesoscale Motions to the Mass and Heat Fluxes of an Intense Tropical Convective System, Journal of Atmospheric Sciences, 37, 784 – 796, https://doi.org/10.1175/1520-0469(1980)037<0784:TCOMMT>2.0.CO;2, 1980.

LeMone, M. A. and Zipser, E. J.: Cumulonimbus Vertical Velocity Events in GATE. Part I: Diameter, Intensity and Mass Flux, Journal of Atmospheric Sciences, 37, 2444–2457, https://doi.org/10.1175/1520-0469(1980)037<2444:CVVEIG>2.0.CO;2, 1980.

Li, W., Zhang, F., Yu, Y., Iwabuchi, H., Shen, Z., Wang, G., and Zhang, Y.: The semi-diurnal cycle of deep convective systems over Eastern China and its surrounding seas in summer based on an automatic tracking algorithm, Clim. Dyn., 56, 357–379, https://doi.org/10.1007/s00382-020-05474-1, 2021.

Liu, C. and Zipser, E. J.: Diurnal cycles of precipitation, clouds, and lightning in the tropics from 9 years of TRMM observations, Geophysical Research Letters, 35, L04 819, https://doi.org/https://doi.org/10.1029/2007GL032437, 2008.

Luo, Z., Liu, G. Y., and Stephens, G. L.: CloudSat adding new insight into tropical penetrating convection, Geophys. Res. Lett., 35, L19 819, https://doi.org/10.1029/2008GL035330, 2008.

Machado, L. A. T., Rossow, W. B., Guedes, R. L., and Walker, A. W.: Life Cycle Variations of Mesoscale Convective Systems over the Americas, Monthly Weather Review, 126, 1630 – 1654, https://doi.org/10.1175/1520-0493(1998)126<1630:LCVOMC>2.0.CO;2, 1998.

Maddox, R. A.: Mesoscale Convective Complexes, BAMS, 61, 1374–1387, https://doi.org/https://doi.org/10.1175/1520-0477(1980)061<1374:MCC>2.0.CO;2, 1980.

Marchand, R., Mace, G. G., Ackerman, T., and Stephens, G.: Hydrometeor Detection Using Cloudsat—An Earth-Orbiting 94-GHz Cloud Radar, J. Atmos. Oceanic Tech., 25, 519–533, https://doi.org/10.1175/2007JTECHA1006.1, 2008.

Masunaga, H. and Luo, Z. J.: Convective and large-scale mass flux profiles over tropical oceans determined from synergistic analysis of a suite of satellite observations, J. Geophys. Res. Atmos., 121, https://doi.org/10.1002/2016JD024753, 2016.

Mecikalski, J. R., MacKenzie, W. M., Koenig, M., and Muller, S.: Cloud-Top Properties of Growing Cumulus prior to Convective Initiation as Measured by Meteosat Second Generation. Part I: Infrared Fields, JAMC, 49, 521–534, https://doi.org/10.1175/2009JAMC2344.1, 2010.

Meyer, F.: Topographic distance and watershed lines, Signal Process., 38, 113–125, https://doi.org/10.1016/0165-1684(94)90060-4, 1994.

Nesbitt, S. W. and Zipser, E. J.: The Diurnal Cycle of Rainfall and Convective Intensity according to Three Years of TRMM Measurements, Journal of Climate, 16, 1456 – 1475, https://doi.org/10.1175/1520-0442(2003)016<1456:TDCORA>2.0.CO;2, 2003.

Nicholson, S. E.: The ITCZ and the Seasonal Cycle over Equatorial Africa, BAMS, 99, 337–348, https://doi.org/10.1175/BAMS-D-16-0287.1, 2018.

Oreopoulos, L., Cho, N., and Lee, D.: New insights about cloud vertical structure from CloudSat and CALIPSO observations, J. Geophys. Res. Atmos., 122, 9280–9300, https://doi.org/10.1002/2017JD026629, 2017.

Orlanski, I.: A Rational Subdivision of Scales for Atmospheric Processes, BAMS, 56, 527–530, https://www.jstor.org/stable/26216020, 1975.

Patra, S. and Kalapureddy, M.: Cloud radar observations of multi-scale variability of cloud vertical structure associated with Indian summer monsoon over a tropical location, Clim. Dyn., 56, https://doi.org/10.1007/s00382-020-05520-y, 2021.

Pilewskie, J. A. and L'Ecuyer, T. S.: The Global Nature of Early-Afternoon and Late-Night Convection Through the Eyes of the A-Train, Journal of Geophysical Research: Atmospheres, 127, e2022JD036 438, https://doi.org/https://doi.org/10.1029/2022JD036438, 2022.

Prein, A. F., Feng, Z., Fiolleau, T., Moon, Z. L., Núñez Ocasio, K. M., Kukulies, J., Roca, R., Varble, A. C., Rehbein, A., Liu, C., Ikeda, K., Mu, Y., and Rasmussen, R. M.: Km-Scale Simulations of Mesoscale Convective Systems Over South America—A Feature Tracker Intercomparison, J. Geophys. Res. Atmos., 129, e2023JD040 254, https://doi.org/10.1029/2023JD040254, 2024.

Raut, B. A., Jackson, R., Picel, M., Collis, S. M., Bergemann, M., and Jakob, C.: An Adaptive Tracking Algorithm for Convection in Simulated and Remote Sensing Data, JAMC, 60, 513–526, https://doi.org/10.1175/JAMC-D-20-0119.1, 2021.

Roca, R., Bergès, J.-C., Brogniez, H., Capderou, M., Chambon, P., Chomette, O., Cloché, S., Fiolleau, T., Jobard, I., Lémond, J., Ly, M., and Picon, L.: On the water and energy cycles in the Tropics, CR GEOSCI, 342, 390–402, https://doi.org/10.1016/j.crte.2010.01.003, 2010.

Ronneberger, O., Fischer, P., and Brox, T.: U-Net: Convolutional Networks for Biomedical Image Segmentation, in: Medical Image Computing and Computer-Assisted Intervention – MICCAI 2015, edited by Navab, N., Hornegger, J., Wells, W. M., and Frangi, A. F., vol. 9351, pp. 234–241, Springer International Publishing, Cham, 2015.

Sassen, K. and Wang, Z.: Classifying clouds around the globe with the CloudSat radar: 1-year of results, Geophys. Res. Lett., 35, L04 805, https://doi.org/10.1029/2007GL032591, 2008.

Schmetz, J., Pili, P., Tjemkes, S., Just, D., Kerkmann, J., Rota, S., and Ratier, A.: An introduction to Metetsat second generation (MSG), BAMS, 83, 977–992, https://doi.org/10.1175/1520-0477(2002)083<0977:AITMSG>2.3.CO;2, 2002.

Semie, A. G. and Bony, S.: Relationship Between Precipitation Extremes and Convective Organization Inferred From Satellite Observations, Geophys. Res. Lett., 47, e2019GL086 927, https://doi.org/10.1029/2019GL086927, 2020.

Sherwood, S. C., Webb, M. J., Annan, J. D., Armour, K. C., Forster, P. M., Hargreaves, J. C., Hegerl, G., Klein, S. A., Marvel, K. D., Rohling, E. J., Watanabe, M., Andrews, T., Braconnot, P., Bretherton, C. S., Foster, G. L., Hausfather, Z., von der Heydt, A. S.,

Knutti, R., Mauritsen, T., Norris, J. R., Proistosescu, C., Rugenstein, M., Schmidt, G. A., Tokarska, K. B., and Zelinka, M. D.: An Assessment of Earth's Climate Sensitivity Using Multiple Lines of Evidence, Reviews of Geophysics, 58, e2019RG000 678, https://doi.org/https://doi.org/10.1029/2019RG000678, 2020.

Sokolowsky, G. A., Freeman, S. W., Jones, W. K., Kukulies, J., Senf, F., Marinescu, P. J., Heikenfeld, M., Brunner, K. N., Bruning, E. C., Collis, S. M., Jackson, R. C., Leung, G. R., Pfeifer, N., Raut, B. A., Saleeby, S. M., Stier, P., and van den Heever, S. C.: *tobac* v1.5: introducing fast 3D tracking, splits and mergers, and other enhancements for identifying and analysing meteorological phenomena, Geosci. Model Dev., 17, 5309–5330, https://doi.org/10.5194/gmd-17-5309-2024, 2024.

Steiner, M., Houze, R. A., and Yuter, S. E.: Climatological Characterization of Three-Dimensional Storm Structure from Operational Radar and Rain Gauge Data, JAMC, 34, 1978–2007, https://doi.org/10.1175/1520-0450(1995)034<1978:CCOTDS>2.0.CO;2, 1995.

Stephens, G. L., Vane, D. G., Tanelli, S., Im, E., Durden, S., Rokey, M., Reinke, D., Partain, P., Mace, G. G., Austin, R., L'Ecuyer, T., Haynes, J., Lebsock, M., Suzuki, K., Waliser, D., Wu, D., Kay, J., Gettelman, A., Wang, Z., and Marchand, R.: CloudSat mission: Performance and early science after the first year of operation, J. Geophys. Res. Atmos., 113, https://doi.org/10.1029/2008JD009982, 2008.

Takahashi, H. and Luo, Z.: Where is the level of neutral buoyancy for deep convection?, Geophysical Research Letters, 39, L15 809, https://doi.org/https://doi.org/10.1029/2012GL052638, 2012.

Takahashi, H., Luo, Z. J., and Stephens, G. L.: Level of neutral buoyancy, deep convective outflow, and convective core: New perspectives based on 5 years of CloudSat data, J. Geophys. Res. Atmos., 122, 2958–2969, https://doi.org/10.1002/2016JD025969, 2017.

Takahashi, H., Luo, Z. J., Stephens, G., and Mulholland, J. P.: Revisiting the Land-Ocean Contrasts in Deep Convective Cloud Intensity Using Global Satellite Observations, Geophys. Res. Lett., 50, e2022GL102 089, https://doi.org/10.1029/2022GL102089, 2023.

Taylor, C. M., Klein, C., Dione, C., Parker, D. J., Marsham, J., Diop, C. A., Fletcher, J., Chaibou, A. A. S., Nafissa, D. B., Semeena, V. S., Cole, S. J., and Anderson, S. R.: Nowcasting tracks of severe convective storms in West Africa from observations of land surface state, Environ. Res. Lett., 17, 034 016, https://doi.org/10.1088/1748-9326/ac536d, 2022.

Taylor, S., Stier, P., White, B., Finkensieper, S., and Stengel, M.: Evaluating the diurnal cycle in cloud top temperature from SEVIRI, Atmos. Chem. Phys., 17, 7035–7053, https://doi.org/10.5194/acp-17-7035-2017, 2017.

Tomkins, L. M., Yuter, S. E., and Miller, M. A.: Dual adaptive differential threshold method for automated detection of faint and strong echo features in radar observations of winter storms, Atmos. Meas. Tech., 17, 3377–3399, https://doi.org/10.5194/amt-17-3377-2024, 2024.

Vondou, D. A.: Spatio-Temporal Variability of Western Central African Convection from Infrared Observations, Atmos., 3, 377–399, https://doi.org/10.3390/atmos3030377, 2012.

Wall, C. J., Norris, J. R., Gasparini, B., Smith, W. L., Thieman, M. M., and Sourdeval, O.: Observational Evidence that Radiative Heating Modifies the Life Cycle of Tropical Anvil Clouds, J. Clim., 33, 8621–8640, https://doi.org/10.1175/JCLI-D-20-0204.1, 2020.

Wang, X., Cui, C., Cui, W., and Shi, Y.: Modes of mesoscale convective system organization during Meiyu season over the Yangtze River basin, Acta Meteorol. Sin., 28, 111–126, https://doi.org/10.1007/s13351-014-0108-4, 2014.

Wielicki, B. A., Cess, R. D., King, M. D., Randall, D. A., and Harrison, E. F.: Mission to Planet Earth: Role of Clouds and Radiation in Climate, BAMS, 76, 2125 – 2154, https://doi.org/10.1175/1520-0477(1995)076<2125:MTPERO>2.0.CO;2, 1995.

Wilcox, E. M., Yuan, T., and Song, H.: Deep convective cloud system size and structure across the global tropics and subtropics, Atmos. Meas. Tech., 16, 5387–5401, https://doi.org/10.5194/amt-16-5387-2023, 2023.

Yuter, S. E., Houze, R. A., Smith, E. A., Wilheit, T. T., and Zipser, E.: Physical Characterization of Tropical Oceanic Convection Observed in KWAJEX, J. Appl. Meteorol., 44, 385–415, https://www.jstor.org/stable/26185647, 2005.

Zipser, E. J. and LeMone, M. A.: Cumulonimbus Vertical Velocity Events in GATE. Part II: Synthesis and Model Core Structure, Journal of Atmospheric Sciences, 37, 2458–2469, https://doi.org/10.1175/1520-0469(1980)037<2458:CVVEIG>2.0.CO;2, 1980.

Zipser, E. J., Cecil, D. J., Liu, C., Nesbitt, S. W., and Yorty, D. P.: Where are the most intense thunderstorms on earth?, BAMS, 87, 1057–1072, https://doi.org/10.1175/BAMS-87-8-1057, 2006.